

1 Lithological, petrophysical and seal properties of mass-transport
2 complexes (MTCs), northern Gulf of Mexico

3 Nan Wu¹, Christopher A-L. Jackson¹, Howard D. Johnson¹, David M. Hodgson²

4 ¹Basins Research Group, Department of Earth Science & Engineering, Imperial College, Prince
5 Consort Road, London, SW7 2BP, UK

6 ²School of Earth and Environment, University of Leeds, Leeds, LS2 9JT, UK

7 *Email: n.wu16@imperial.ac.uk

8 Abstract

9 Mass transport complexes (MTCs) are one of the most sedimentologically and seismically
10 distinctive depositional elements in deep-water depositional systems. Seismic reflection data
11 provide spectacular images of their structure, size, and distribution, although a lack of
12 borehole data means there is limited direct calibration between MTC lithology and
13 petrophysical expression, or knowledge of how they may act as hydrocarbon reservoir seals.
14 In this study, we evaluate the lithological and petrophysical properties, and seismic
15 characteristics of three deeply-buried (>2300 m/7546 ft below the seabed), Pleistocene MTCs
16 in the northern Gulf of Mexico. We show that: (i) MTC lithology is highly variable, comprising
17 a mudstone-rich debrite matrix containing large (4.5 km³/1.08 mi³), deformed, sandstone-
18 rich blocks; (ii) MTCs are generally acoustically faster and are more resistive than lithologically
19 similar (i.e. mudstone-dominated) slope deposits occurring at a similar burial depth; (iii) MTC
20 velocity and resistivity increase with depth, likely reflecting an overall downward increase in
21 the degree of compaction; and (iv) the lowermost 15-30 m (49-98 ft) of the MTCs, which

22 represent the basal shear zones, are characterised by relatively high P-wave velocity and
23 resistivity values, likely due to shear-induced over-compaction. We conclude that detailed
24 analysis of petrophysical data, in particular velocity and resistivity logs, may allow recognition
25 of MTCs in the absence of high-quality seismic reflection data, including explicit identification
26 of the basal shear zone. Furthermore, the relatively thick basal shear zone, rather than the
27 overlying and substantially thicker MTC itself, may form the primary permeability barrier and
28 thus seal for underlying hydrocarbon accumulations.

29 1 Introduction

30 Mass-transport complexes (MTCs) comprise deposits from a range of weakly turbulent to fully
31 cohesive, plug-like sediment gravity flows such as slides, slumps, and debris-flows (Talling et
32 al., 2012). MTCs are one of the most sedimentological and seismically distinctive depositional
33 elements in deep-water depositional systems, where they may form a key component of the
34 stratigraphic record (Posamentier and Martinsen, 2011). MTCs may represent geohazards,
35 threatening seabed infrastructure, and can generate seabed topography that controls the
36 dispersal of subsequent sediment gravity-currents (Martinsen, 1989; Hühnerbach and
37 Masson, 2004; Solheim et al., 2005; Lee et al., 2007; Sawyer, 2007; Urgeles and Camerlenghi,
38 2013; Kneller et al., 2016). MTCs may also represent drilling hazards because of unpredictable
39 intraformational pressures, and can slow down the penetration rate of suction anchor piles
40 and jetted conductors, thus leading to non-productive time (Shipp et al., 2004). In addition,
41 MTCs may form hydraulic seals to hydrocarbon accumulations hosted in underlying (or
42 laterally equivalent) sandstone reservoirs (Piper et al., 1997; Shipp, 2004; Sawyer et al., 2009;
43 Algar et al., 2011), or form reservoir themselves (Meckel III, 2011). The composition and

44 distribution of MTCs, and our ability to recognise them in the subsurface, are thus of concern
45 to the hydrocarbon industry.

46 Typically, MTCs are studied in the subsurface using seismic reflection data (e.g. Prather et al.,
47 1998; Posamentier and Kolla, 2003; Frey Martinez et al., 2005; Posamentier, 2005;
48 Moscardelli et al., 2006; Moscardelli and Wood, 2008; Bull et al., 2009; Moernaut and De
49 Batist, 2011; Ortiz-Karpf et al., 2015; Ortiz - Karpf et al., 2016), or in the field (e.g. Martinsen
50 et al., 2003; Jackson and Johnson, 2009; Dykstra et al., 2011; King et al., 2011; Shipp et al.,
51 2011; Alves, 2015; Sobiesiak et al., 2016; Hodgson et al., 2018). Seismic reflection data allow
52 determination of the distribution, external geometry, internal structure, and kinematics of
53 MTCs. However, these data do not provide a direct calibration of MTC lithology, which must
54 instead be inferred from seismic facies analysis (Moscardelli et al., 2006; Madof et al., 2009;
55 Perov and Bhattacharya, 2011). In contrast, field-based studies permit detailed analysis of
56 MTC structure and lithology, but these exhumed and weathered systems do not permit a
57 direct petrophysical characterisation. In addition, the field-based studies may not permit a
58 fully three-dimensional analysis of very large (i.e. tens to several hundreds of metres thick, by
59 several hundreds of kilometres in areal extent) MTCs, and/or may not reveal their basal and
60 upper surfaces.

61 Integrated petrophysical and lithological studies of buried MTCs are relatively rare, typically
62 drawing on data collected from shallowly buried (<1400 m/4593 ft) deposits (e.g. Sawyer,
63 2007; Flemings et al., 2008; Sawyer et al., 2009; Algar et al., 2011; Dugan, 2012). These studies
64 show that MTCs can be very fine-grained, and may be acoustically faster (and thus more rigid)
65 and have higher resistivity (and thus lower porosity) than surrounding, *in-situ* deep-water
66 sediment of similar composition (Piper et al., 1997; Shipp, 2004; Sawyer, 2007; Algar et al.,

2011; Dugan, 2012). How these properties vary with depth, and how deeply-buried MTCs are expressed in petrophysical data at depths of interest to the hydrocarbon industry, is poorly understood. An exception to this is presented by Algar et al. (2011), who used borehole data to study several deeply buried MTCs offshore NW Borneo; however, in this example they lacked access to high-resolution 3D seismic data to link seismic facies with lithology and petrophysical properties.

In this study, we use 3D seismic reflection and borehole data from the Atwater Valley protraction area of the northern Gulf of Mexico to investigate the relationship between the 3D seismic reflection and petrophysical expression of three deeply (1900 m- 3100 m) buried MTCs, especially the top and base surfaces of MTCs. By doing this, we can improve our ability to use such data to predict their subsurface rock properties and associated fluid flow behaviour.

2 Geological setting

Our study area is located in Block 8 of the Atwater Valley concession, c. 130 km (80.8 mi) SW of the modern Mississippi delta mouth, and c. 60 km (37.3 mi) basinward of the Pleistocene shelf edge (Galloway et al., 2000; Galloway, 2001) (Figure 1). Present water depths range from 1150 m (3773 ft) in the SE to 650 m (2133 ft) in the NW. The northern Mississippi slope comprises a series of salt diapirs and minibasins formed due to flow of the Jurassic Louann Salt (Martin and Bouma, 1982; Peel et al., 1995). This study focuses on Pleistocene sediments preserved within minibasins formed by subsidence into allochthonous salt (Jackson et al., 2018) (Figure 1). During the Early to Middle Pleistocene, the Mississippi River and its tributaries supplied the Mississippi delta, which delivered significant amounts of sediment to the shelf, slope, and basin-floor (Galloway et al., 2000; Galloway, 2008; Galloway et al., 2011).

90 In the Late Pleistocene, the East Mississippi river merged with the Red River, forming a deeply
91 incised, pro-glacial Mississippi valley (Saucier, 1997; Galloway et al., 2000). This valley, and
92 the downdip Mississippi canyon, represented the main conduit for sediment transfer onto
93 the basin floor (Weimer et al., 1998; Galloway et al., 2000; Winker and Booth, 2000).

94 A seabed map (Figure 2A) and a top salt depth map (Figure 2B) highlight the main salt
95 structures and minibasins within the study area. This study focuses on the stratigraphic fill of
96 an N-S trending, up to 21 km (13 mi) long and 10 km (6.2 mi) wide minibasin that contains a
97 3.5 km (2.2 mi) thick succession of Pleistocene siliciclastics (minibasin 5; Figure 2A and 2B).
98 Biostratigraphic data provide relatively low-resolution age control for the Cenozoic sediments
99 (Figure 3B).

100 3 Dataset and Methods

101 The seismic dataset was acquired in 1995-1998, and reprocessed as a single survey in 2008. It
102 is a 3D zero-phase, Kirchhoff pre-stack depth-migrated seismic reflection volume, with a
103 vertical sample rate of 10 m (32.8 ft), record length (depth) of 15 km (9.32 mi), and final bin
104 size of 25 m x 25 m (82 ft x 82 ft). The dataset covers an area of approximately 550 km² (212.4
105 mi²) in the southwestern Mississippi Canyon (MC) and northwestern Atwater Valley (AT)
106 protraction areas of the east-central Gulf of Mexico (Figure 2). A downward increase and
107 decrease in acoustic impedance is expressed as red (positive) and blue (negative) reflection
108 events, respectively. The estimated vertical seismic resolution in the interval of interest
109 ranges from 17-27 m (55.8-88.6 ft). A slightly deviated exploration well (AT-8 #1 ST) was
110 drilled in 1997 in the east of the study area, encountering a c. 3600 m (11811 ft) thick
111 succession of Pleistocene deep-water clastic succession (Figure 2) (see Jackson et al., 2018 for
112 details of the biostratigraphic data). The well-log dataset includes measurements of velocity

113 (Sonic), gamma-ray (GR) and resistivity (RT). Shale volume (Vsh) was calculated based on the
114 GR response using the following equation:

$$115 \quad V_{sh} = \frac{GR_{log} - GR_{min}}{GR_{max} - GR_{min}}$$

116 P-wave velocity (Vp) was calculated based on the sonic (DT) response using the following
117 equation:

$$118 \quad V_p = \frac{1}{Sonic} * 10^6 \text{ m/s}$$

119 We mapped eight highly reflective (i.e. reflections picked on high amplitude peaks or troughs),
120 laterally continuous seismic horizons (H0 to seabed; Figure 3B) that delineate several MTCs
121 preserved in minibasin 5. The MTCs are imaged using a combination of geometric, amplitude
122 and frequency based variance and chaos attributes. The variance attribute was calculated
123 based on the Van Bommel and Pepper (2000) edge detection method; this converts the
124 amplitude-based seismic volume into a reflection discontinuity volume that is particularly
125 useful for highlighting structural (e.g. faults) and stratigraphic (e.g. the abrupt seismic facies
126 change from chaotic MTCs to more continuous slope strata). The chaos attribute was
127 measured in using dip and azimuth estimation method; like variance, chaos highlights abrupt
128 changes in seismic facies, and it was also used for mapping structural and stratigraphic
129 discontinuities (Chopra and Marfurt, 2007; Brown, 2011; Koson et al., 2014).

130 Where available, we used density and sonic log data to generate a synthetic seismogram to
131 tie seismic and borehole data. This allowed a direct assessment of the lithology and
132 petrophysical properties of the MTCs, as well as their bounding strata. The horizons used for
133 the QC are the salt weld horizon and a high amplitude peak above the salt weld (see
134 supplementary martial 1). Because the calliper log is only available in the section below the

135 salt weld, the hole conditions, and thus quality of the extracted log data in the interval of
136 interest, can only be constrained using the ROP (rate of penetration) log (see supplementary
137 material 2A). The ROP log is relatively smooth, suggesting the hole conditions and well-log
138 data in the interval of interest are relatively good. For example, the ROP log is relatively
139 smooth, increasing from 0.004 to 0.008 m/s from sea-level to 2750 m and 0.008 to 0.0125
140 m/s from 2750 m to 3800 m. This suggests that the hole conditions and well-log data in the
141 interval of interest are relatively good. The overall trends seen are logically related to
142 increasing burial compaction in the MTC intervals (see supplementary material 2B); and the
143 variations characterising the BSZ occur over a short length-scale, and it seems unlikely that
144 they all represent poor hole conditions at this specific depth.

145 Five MTC-bearing intervals were drilled and logged by AT-8 #1 ST; due to the lack of well data
146 for the shallowest MTCs, we here analyse only three (Figure 3B). Well-log data (i.e., GR, Sonic
147 and RT) were used to infer the lithology of the MTCs and their bounding strata. Cross-plots
148 were constructed to examine the petrophysical-property variations within MTC-bearing
149 intervals and bounding strata.

150 4 Seismic facies analysis

151 A regional N-S trending seismic profile through minibasin 5 illustrates the geometry of the
152 depocentre and bounding salt structures (Figure 3A). We see two main seismic reflection
153 configurations: (i) *chaotic*, which are interpreted as MTCs (i.e. remobilised strata); and (ii)
154 *continuous*, which are interpreted as slope deposits (i.e. in-situ strata) (Figure 3C) (Prather et
155 al., 1998; Roesink et al., 2004; Sincavage et al., 2004; Madof et al., 2009; Doughty-Jones et al.,
156 2017). The seismic facies characteristics of the MTCs (facies 3.1 and 3.2) and slope deposits
157 (facies 1 and 2) are further classified based on a more detailed analysis of their seismic

158 reflection characteristics, and by comparing their expression (e.g. reflectivity and continuity,
159 and their external and internal geometry) with previous seismic facies analysis schemes
160 developed for age-equivalent (i.e. Plio-Pleistocene) deep-water sediments deposited in
161 nearby areas (Prather et al., 1998; Sawyer et al., 2007; Madof et al., 2009). We here briefly
162 describe the observed seismic facies and their GR expression (see also Table 1), before we
163 provide a more detailed analysis of the petrophysical expression of the MTC-bearing intervals.

164 4.1 Seismic facies 1 (SF1)

165 SF1 comprises sub-parallel to parallel, moderate continuity, high-amplitude reflections. SF1 is
166 c. 40-50 m (131-164 ft) thick, and has flat upper and lower contacts with bounding deposits
167 (Table 1). SF1 has a blocky, low GR response at its base, and a serrated, higher GR response
168 at its top, displaying an overall fining-upward trend. Based on its log response and previous
169 seismic facies-based studies, we infer that SF1 represents thinly bedded, sandstone-rich (at
170 its base) and mudstone-rich (at its top) deposits, possibly deposited in a channel-levee system
171 or at the fringes of a lobe complex (Table 1). SF1 is thus comparable with C_{th} facies of Prather
172 et al. (1998), with similar seismic facies being documented by Roesink et al. (2004), Sincavage
173 et al. (2004), and Madof et al. (2009) (i.e. inter-bedded sandstone- and mudstone-rich
174 turbidites).

175 4.2 Seismic facies 2 (SF2)

176 SF2 is c. 100-170 m (328.1-557.7 ft) thick, and is bounded by sub-parallel to parallel, relatively
177 continuous, low-to-medium amplitude reflections. It comprises laterally continuous, parallel,
178 low- to medium amplitude reflections (Table 1). SF2 displays a high GR response, suggesting
179 it is mudstone-dominated. Based on its expression in seismic and borehole data, and by
180 comparison to seismic facies interpreted in other studies, we infer SF2 represents low-energy,

181 'background-type' slope deposits, comprising mudstone-rich hemipelagic deposits that may
182 be interbedded with very thin turbidites (Prather et al., 1998; Madof et al., 2009; Perov and
183 Bhattacharya, 2011).

184 4.3 Seismic facies 3.1 (SF3.1)

185 SF3.1 is c. 150-180 m (492-590 ft) thick, has a rugose top surface and a flat base (Table 1), and
186 comprises moderately deformed, folded and faulted, medium-to-high amplitude seismic
187 reflections. SF3.1 is characterised by a bell-shaped GR response, with a fining upward trend
188 near its bottom, and box-shaped, 80-120 m (262-393 ft) thick intervals of low GR at its middle
189 and top. The lower part of SF3.1 is dominated by high GR intervals and is inferred to be
190 mudstone-rich. In contrast, the middle and upper parts of SF3.1 are characterised by low GR
191 values, and are inferred to be sandstone-rich, with thinly bedded sandstone and mudstone.
192 The abundance of faulting and folding, combined with the rugose upper surface, suggest
193 SF3.1 has been remobilised and transported, most likely within a MTC. Based its sandstone-
194 rich character we propose that SF3.1 was originally deposited in and ultimately sourced from
195 the remobilisation of, submarine lobes (Mahaffie, 1995; Prather et al., 1998; Posamentier and
196 Kolla, 2003; Posamentier, 2005; Sawyer et al., 2007; Doughty-Jones et al., 2017).

197 4.3 Seismic facies 3.2 (SF3.2)

198 SF3.2 comprises c. 190-270 m (623-885 ft) thick packages of chaotic, low-to-moderate
199 amplitude seismic reflections. The top of SF3.2 is rugose, whereas its basal contact is relatively
200 flat (Table 1). SF3.2 is characterised by a serrated, overall high GR response that locally
201 contains sharp-based, box-shaped, low GR intervals (Table 1). SF3.2 is therefore interpreted
202 to be mudstone-dominated (i.e. high GR intervals) and more specifically, based on its seismic
203 and log response, and interpretations arising from previous seismic facies-based studies

204 (Prather et al., 1998; Sawyer, 2007; Madof et al., 2009; Perov and Bhattacharya, 2011), as a
205 mudstone-rich debrite. Sandstone-rich intervals (i.e. low GR intervals) are inferred to be
206 sandstone blocks encased within the very fin-grained debrite matrix.

207 5. Lithology and distribution of MTCs

208 We focus on three MTCs preserved in minibasin 5 (MTC1-3; Figure 3B, 3C), and we begin by
209 providing a description of their general seismic expression and lithology. In subsequent
210 sections we synthesize observations from these three MTCs to investigate their detailed
211 petrophysical response, and how this relates to MTC structure and emplacement.

212 5.1 MTC 1

213 *Geometry and seismic facies*

214 MTC 1 is bound by horizon H1 and H2 (Figure 3B). It has a tongue-shaped external form,
215 widening towards the SE, away from diapir A (Figure 4A, 4B). MTC 1 is up to 270 m (885 ft)
216 thick, being thickest in the minibasin centre. A 180 m (590 ft) high, 6 km (3.7 mi) long erosion
217 surface separates MTC 1 from an overlying debrite (SF3.2), and an underlying interval that
218 contains folded and faulted blocks (Figure 4C, 4D). The abundance of faulting and folding,
219 combined with scours along the basal surface (Figure 4C), suggest that large blocks were
220 transported within MTC1. These blocks are defined by packages of SF3.1 and SF1 that are 80-
221 180 m (262-590 ft) thick, 4.5-6.8 km (2.8-4.2 mi) long, and 2-3.6 km (1.2-2.2 mi) wide, and
222 which contain NE-SW-striking thrusts. The well intersects the distal part of MTC 1, in a location
223 where thrusts and folds occur (Figure 4A).

224 *Lithology*

225 MTC 1 is sandstone-rich (SF3.1) near its base and mudstone-rich (SF3.2) at its top (Figure 5A).

226 To better investigate lithology variations associated with the three constituent seismic facies
227 of MTC 1, we generated a cross-plot of shale volume (Vsh) and velocity (Vp) (Figure 5B).

228 This plot shows that: (1) both SF1 and SF3.1 is heterogeneous, containing both sandstone-
229 and mudstone-rich intervals; SF3.1 contains minor amounts of muddy sandstone, whereas
230 SF1 does not; (2) sandstone-rich deposits associated with SF1 and SF3.1 are capped and
231 surrounded by mudstone-rich debrite, an observation also inferred from their seismic
232 expression (Figure 4C, 4D); and (3) SF3.2 is mudstone-dominated, can be clearly differentiated
233 from other seismic facies, and is defined by a relatively narrow distribution in the cross plot.

234 5.2 MTC 2

235 *Geometry and seismic facies*

236 We infer MTC 2 comprises two separate, debrite-dominated (i.e. SF3.2) deposits (MTC 2.1
237 and 2.2; Figure 6A, 6B), separated by a through-going seismic horizon H2.2 (Figure 6C, 6D).
238 Taken together, MTC 2.1 and 2.2 define an up to 120 m (393.7 ft) thick, N-S trending,
239 lenticular-shaped body that widens slightly northwards (Figure 6B). Two bodies in the centre
240 of the minibasin have sharp, sub-vertical contacts with MTC 2.1, and are interpreted as
241 remnant blocks (Figure 6C, 6D). The well interests the middle part of MTC 2, in a location
242 where it is dominated by SF3.2 (Figure 6A).

243 *Lithology*

244 The remnant block is mudstone-rich at its base, and comprises sandstone and mudstone
245 towards its top (Figure 7A). Overlying MTCs are mudstone-dominated (MTC 2.1 and 2.2;

246 Figure 7A), although the lithological composition of MTC 2 varies when observed in the cross-
247 plot of shale volume (Vsh) and velocity (Vp) (Figure 7B). For example: (1) SF1 and SF3.2 are
248 mudstone-dominated, with a small portion of sandstone-rich deposits, although the former
249 is more mudstone-rich than the latter; (2) SF2 is mudstone-rich, containing some muddy
250 sandstone; and (3) sandstone-rich deposits associated with SF1 are capped and surrounded
251 by mudstone-rich debrite and undeformed background deposits. A similar stratigraphic
252 relationship is inferred from the seismic data (Figure 6C, 6D).

253 5.3 MTC 3

254 *Geometry and seismic facies*

255 MTC 3 occurs in the centre of the minibasin, is slightly elongate, and trends north (Figure 8A,
256 8B). MTC 3 is bounded by horizon H4 and H4.1 (Figure 3B), is up to 182 m (597 ft) thick,
257 comprises chaotic, moderate-amplitude reflections (SF3.2), and has a flat base and rugose top
258 (Figure 8C, 8D). The well intersects the central part of MTC 3, in a region where it is dominated
259 by chaotic seismic facies (Figure 8A).

260 *Lithology*

261 MTC 3 has a mudstone-rich base and top, and a sandstone-rich middle (Figure 9A). The
262 composition of MTC 3 is further revealed in a cross-plot of Vsh and Vp (Figure 9B). SF3.2 is
263 dominated by sandstone-rich and mudstone-rich deposits, with a small proportion of muddy
264 sandstone. The lithology of SF3.2 in MTC 3 is thus comparable to that observed in MTC 2, but
265 different to that in MTC 1. Based on seismic and log data, MTC 3 is interpreted as a debrite-
266 dominated MTC containing large, sandstone-rich (c. 70 m/229.7 ft in thickness) blocks.

267 6 Petrophysical analysis of MTCs

268 6.1 General variations in velocity and resistivity

269 Velocity (V_p) data from MTCs 1-3 show that: (i) MTCs are generally characterised by an overall
270 downward increase in V_p (e.g. 2340-2487 m/7677-8159 ft, MTC3 in Figure 10A); (ii)
271 mudstone-dominated parts of MTCs are acoustically faster than similar lithologies at similar
272 burial depths (e.g. the mudstone-rich debrite in MTC 3 is acoustically faster than the overlying
273 and underlying background mudstone-rich deposits; 2300-2550 m/7545.9-8366 ft in Figure
274 10A); (iii) sandstone-dominated parts of all three MTCs tend to have a relatively low V_p , and
275 are acoustically slower than the overlying and underlying mudstone-rich debrite (see below);
276 (iv) the uppermost 8-15 m (26-49 ft) of the MTCs, which are dominated by mudstone-rich
277 sediments and directly underlie the top surface, are 3%-5% acoustically faster than similar
278 material within the overlying background deposits (Figure 10A); and (v) the lowermost 15-30
279 m (49-98 ft) of the MTCs, which are invariably mudstone-dominated and which directly
280 overlie the seismically defined base of the MTC, are 5%-9% and 7-25% acoustically faster than
281 similar material within the overlying MTCs and underlying background deposits, respectively.
282 The reasons for the sharp increase in V_p just above the MTC basal shear surface is discussed
283 further below.

284 Resistivity (RT) log data show that: (i) RT increases downward within MTCs, but decreases
285 downward in lithologically similar slope deposits in bounding intervals (e.g. increases from
286 2770-2890 m/9087.9-9481.6 ft in MTC2, and decreases from 2890-3080 m/9481.6-10104.9 ft
287 in the underlying remnant block, Figure 10B); (ii) mudstone-rich debrite (SF3.2) are typically
288 more resistive than surrounding, undeformed background deposits at similar burial depths
289 (e.g., 3075-3100 m/ 10088.6- 10170.6 ft in MTC1 Figure 10B); (iii) sandstone-dominated parts

290 of all three MTCs tend to have a relatively low RT, and are less resistive than overlying and
291 underlying mudstone-rich debrite (see below); (iv) RT response within MTC 2 and MTC 3 are
292 lower than surrounding, undeformed, background deposits; (v) the uppermost 8-15 m (26-49
293 ft) MTCs 1 and 2 are characterised by RT values 30%-45% higher than overlying background
294 deposits; and (vi) the lowermost 15-30 m (49-98 ft) of the MTCs are characterised by RT values
295 that are 15%-25% higher than would be expected by the downward-increasing, 'background'
296 RT trend response in the overlying MTC, and 16%-30% higher than underlying and thus more
297 deeply buried, slope background deposits (Figure 14). This finding is consistent with previous
298 studies that suggest that RT increases with depth within MTCs (Shipp, 2004; Dugan, 2012),
299 but is counter to other studies which suggest MTCs are typically more resistive than
300 surrounding sediments (Sawyer et al., 2009; Algar et al., 2011). We explore the reasons for
301 this further in the discussion.

302 6.2 Petrophysical and acoustic characteristics of the basal shear zone 303 and the top surface

304 The term basal shear surface (BSS) is defined by (Varnes, 1978) as a discrete seismic reflection
305 defining the base of a relatively chaotic package of seismic reflections (i.e. an MTC). They infer
306 this is the surface across which the MTC was translated and ultimately deposited, containing
307 deformation associated with both these processes (see also Frey Martinez et al., 2005; Bull et
308 al., 2009). In our study, the BSS is characterised by high-amplitude, negative seismic reflection
309 that defines a downward decrease in acoustic impedance and, we infer, a change from
310 acoustically fast MTC-related materials and the pre-MTC slope substrate. Field suggest that,
311 rather than representing a discrete surface, the BSS identified in seismic reflection data
312 instead defines a zone of deformed materials related to MTC transport and emplacement

313 (basal shear zone or 'BSZ' of Hodgson et al., 2018, or 'kinematic boundary layer' of Butler et
314 al., 2016). In detail, the BSZ comprises sediments deformed: (i) wholly within the MTC body
315 during its transport and emplacement; (ii) wholly below the MTC within the pre-emplacement
316 seabed, with strain imposed by shear caused by the overlying travelling mass; or (iii) within
317 and below the travelling mass.

318 Our petrophysical data allow us to identify a 15-30 m thick zone define by relatively high VP
319 and RT at the base of the MTCs. We interpret this interval represents the basal BSZ. These
320 petrophysically defined zones are represented in seismic data by a seemingly discrete surface
321 due to the limited vertical resolution of the latter (e.g. the 15 m thick BSZ of MTC 1 is only
322 represented by a single trough reflection in seismic data). We propose that the BSZ could
323 represent sediments that wholly within the MTCs, deposited at the lowermost section which
324 has highest VP and RT response.

325 The BSSs of all three MTCs are all characterised by negative, medium-to-high amplitude
326 seismic reflections of moderate continuity (Figure 4D, 6C, 8C). For example, the BSZ of MTC 1
327 is more reflective (i.e. -15701 at point a1 in Figure 11A) than the laterally correlative reflection
328 within flanking background strata (i.e. -4008 at point b1 in Figure 11A). The top surfaces of all
329 three MTCs are characterised by positive, medium-to-high amplitude seismic reflections of
330 poor continuity (Figure 4C, 6C, 8C). For example, the reflection defining the top surface of
331 MTC 1 is at point a2 in Figure 11B is more reflective (i.e. amplitude value of +22387) than the
332 laterally correlative, weaker (-12408), negative amplitude reflection within flanking
333 background strata (i.e. point b2 in Figure 11B).

334 Because amplitude (i.e. reflectivity) is a function of the reflection coefficient (RC) (i.e. acoustic
335 impedance or 'AI' contrasts) and, ultimately, the acoustic properties of rocks, we can explore

336 what lithological combination and/or variations in their physical properties (e.g. compaction)
337 might give rise to the observed seismic response (equation 1):

338
$$RC = \frac{AI_2 - AI_1}{AI_2 + AI_1} \quad (1)$$

339 Where AI_1 and AI_2 are the sediments overlying and underlying the top surface and the BSZ of
340 MTC 1, respectively (Figure 11C). Because the top surface and the BSZ of MTC 1 are more
341 consolidated, they are acoustically faster and more resistive than the overlying and underlying
342 undeformed deposits (i.e. the units directly above and below MTC1 are seismically 'softer')
343 (See Figure 10A, 10B). AI is a function of acoustic velocity (V_p) and density (ρ_b) (equation 2):

344
$$AI = V_p * \rho_b \quad (2)$$

345 Based on this, $AI_2 > AI_1$ across the top surface of MTC 1, and $AI_1 > AI_2$ across the BSZ of MTC 1.
346 This illustrates why: (i) the top surface of MTC 1 is defined by a positive amplitude reflection,
347 whereas the laterally correlative surface, encased within undeformed background deposits,
348 is defined by a negative polarity reflection; and (ii) the amplitude of the BSZ of MTC 1 is not
349 only defined by negative polarity, but is also brighter than that of the laterally correlative,
350 undeformed background deposits.

351 6.3 Petrophysical and acoustic characteristics of sandstone-rich 352 deposit within MTCs

353 MTC 1 has the thickest sandstone-rich interval (c. 170 m/557.7 ft). Sandstone-rich intervals
354 within MTC 2.1, 2.2 and 3 are up to 30 m (98 ft), 10 m (32 ft) and 70 m (229 ft) thick,
355 respectively (Table 2).

356 Overall, in contrast to mudstone-rich parts of MTCs where Vp and RT broadly increase with
357 depth (Figure 12A), sandstone-rich parts of MTCs have variable depth trends (Figure 12B). The
358 sandstone-rich parts of three MTCs have lower average Vp and RT values than the underlying
359 and overlying mudstone-rich debrite (Figure 13). For example, the average Vp value for the
360 sandstone-rich part of MTC 2 is 2140 m/s (7020.9 ft/s). This is lower than the average Vp
361 values of the overlying and underlying mudstone-rich debrites, which are 2210 m/s (7250.7
362 ft/s) and 2240 m/s (7349.1 ft/s), respectively (Fig 13B). The sandstone-rich part of MTC 3
363 displays an overall increase in Vp and RT with depth (Figure 13A), although the sandstone-
364 rich part of MTC 1 does not vary (Figure 13C).

365 The petrophysical properties of sandstone-rich parts of MTC 1 are different to those of
366 surrounding mudstone-rich debrite and sandstone-rich deposits in overlying, undeformed
367 background deposits (Figure 13 C). A simplified Vp depth trend can be proposed based on the
368 observed Vp depth trend in Figure 10A. The MTC intervals, except the sandstone-rich blocks
369 in MTC 1, tend to have relatively high Vp response compared to the overlying and underlying
370 background slope deposits (see also Figure 12A, 12B), which typically exceed the inferred
371 compaction trend. This suggests that MTC intervals, or at least their mudstone-rich sections,
372 are more compacted than and perhaps overcompacted relative to overlying and underlying
373 background slope deposits (Figure 12A). Within MTC 1, the Vp trend of the sandstone-rich
374 blocks shifts sharply to a constant low Vp response as compared to the overlying mudstone-
375 rich debrite that has increasing Vp with depth. This indicates that the sandstone-rich blocks
376 of MTC 1 are *less* compacted than the mudstone-rich, debritic matrix. Furthermore,
377 sandstone-rich blocks are only weakly resistive when compared to the overlying mudstone-
378 rich units (Figure 10, Figure 12, Figure 13C). This may suggest that the sandstone-rich blocks
379 in MTC 1 retain higher porosity and are water-saturated. However, because the MTCs are

380 strongly heterogeneous, the general trends that we describe/interpret in this study may not
381 be specifically tested in this case without a more detailed understanding of the specific
382 consolidation profiles of the muddy vs. sandy lithologies.

383 7 Discussion

384 We have characterised: (i) the lithology of relatively deeply buried, seismic-scale MTCs; (ii)
385 the relationship between MTC seismic facies and lithology; and (iii) the petrophysical
386 properties of MTCs, and how they vary with depth and structural position within individual
387 MTCs. Here, we discuss the key implications of our study.

388 7.1 Lithology of MTCs

389 In this study, we demonstrate that significant amounts of sandstone may be present within
390 MTCs. This sandstone can be surprisingly thick (c. 170 m/557.7 ft), being contained in
391 relatively homogeneous transported blocks (SF3.2), or relatively thin (10-30 m/32.8-98.4 ft),
392 occurring interbedded with mudstone in remobilised lobe and/or channel-fill successions
393 (Table 2). This compositional variability may reflect the different provenance of the MTCs; i.e.
394 from mudstone-rich outer-shelves or slopes lacking sand, or from similar positions that are
395 sandstone-rich due to the presence of deltas or previously deposited, deep-water channel-
396 fills and lobes. MTCs are likely transported along the slope and being laterally bounded by salt
397 diapirs. This contrasts with the widespread occurrence of argillaceous MTCs, such as those
398 encountered in the Nankai Trough (e.g. Strasser et al., 2012), offshore Angola (e.g. Sikkema
399 and Wojcik, 2000) and the Gulf of Mexico (e.g. Shipp, 2004; Flemings et al., 2005; Sawyer et
400 al., 2007; Meckel III, 2011).

401 7.2 Petrophysical properties of MTCs

402 *General Petrophysical properties*

403 Prior well-log based studies from IODP and ODP drilling in the Northern Gulf of Mexico (Shipp
404 et al., 2004; Sawyer, 2007; Sawyer et al., 2009; Dugan, 2012; Flemings et al., 2012) and
405 Northwest Borneo (Algar et al., 2011) show that MTCs tend to have a higher Vp, density and
406 RT values than surrounding non-MTC intervals. This reflects the fact that MTCs are more
407 consolidated than their bounding sediments, an observation that is consistent with
408 geotechnical measurements that indicate shear strength increases, whereas water content
409 and void ratio decrease downward within MTCs (Piper et al., 1997; Shipp et al., 2004; Strong,
410 2009; Long et al., 2011; Alves et al., 2014). Physical experiments and theoretical models (e.g.
411 consolidation, fluid-dynamics, and soil-mechanics) confirm that MTCs are denser than
412 bounding strata, typically being densest within their basal shear zone (Major and Iverson,
413 1999; Sassa et al., 2003; Dugan and Germaine, 2008; Strong, 2009; Meissl et al., 2010).

414 We demonstrate that the three MTCs studied here are more compacted than surrounding
415 background deposits, and that Vp, RT broadly increase downward, and at a higher rate than
416 within underlying and overlying undeformed background sediments. Our findings are thus
417 consistent with observations from Sawyer et al. (2009) and Algar et al. (2011), who show
418 similar downward increase in Vp and RT within individual MTCs. However, RT values are lower
419 than in underlying and overlying undeformed background sediments, except near the MTC
420 basal shear zone. This observation is contrary to previous studies (Shipp, 2004; Sawyer et al.,
421 2009; Dugan, 2012). We note, however, that these authors studied mudstone-dominated
422 MTCs at relatively shallow burial depths (<1400 m/4593 ft), whereas those presented here
423 are relatively sandstone-rich and lie at substantially greater burial depths (>2300 m/7546 ft).

424 The differences observed between these studies may therefore reflect differences in the
425 burial depth and lithology of MTC intervals studied.

426 *Insights into emplacement processes; basal shear surface or zone?*

427 Experimental models show that debrites are typically deposited in response to top-down
428 ‘freezing’ of weakly turbulent, plug-like laminar flows; because the lower parts of these flows
429 are the last to stop deforming they may be more strained (Pickering and Hiscott, 2015). Thin
430 section and outcrop-based studies show evidence of liquefaction and fluidization related
431 structures in the lower part of MTC intervals (Ogata et al., 2014). In this study, we show that
432 the lower 15-30 m (49-98 ft) of the studied MTCs are characterised by relatively high Vp and
433 RT when compared to overlying and underlying deposits. Petrophysical data suggest that,
434 rather than being underlain by a basal shear *surface*, the MTCs overlie a basal shear *zone* (BSZ).
435 BSZ thickness and infer strain (based on Vp value) appears to be positively correlated to the
436 thickness of the overlying MTCs; i.e. the thicker the MTCs, the thicker and more strained the
437 BSZs. For example, MTC 3 and MTC 2 are 170 m (557.7 ft) and 83 m (272 ft) thick, with 30 m
438 (98 ft) and 26 m (85 ft) thick BSZs, respectively. Vp values sharply increase at the BSZs by
439 around 20-25% for each MTC, as compared to the overlying debritic sediments of the main
440 MTC body. This contrasts with MTC 1, where the BSZ is only 15 m (49 ft) thick and where Vp
441 increases by only 7%. These differences in Vp may reflect the fact that the well penetrates: (i)
442 different parts of the different MTCs (i.e. the debritic margin of MTC 1 vs. the debritic centre
443 of MTCs 2 and 3), and (ii) different internal elements of the MTCs (i.e. transported blocks in
444 MTC 1 vs. debris flow matrix in MTCs 2 and 3).

445 Only one well is available for this analysis; however, we can make some observations
446 regarding the lateral variability of petrophysical properties (i.e. Vp and RT) within the three

447 studied MTCs. V_p and the thickness of the BSZs appear to vary laterally, being highest beneath
448 the main body of an MTC (i.e. MTC 2 and MTC 3), and lowest in more distal parts (i.e. MTC 1).
449 This suggests that within a single MTC, the BSZ might be thinnest along its thin margins and
450 thickest beneath its thick centre. However, the thickness and pore pressure of the BSZ might
451 be controlled by other factors, such as: (i) slope angle, which would dictate the momentum
452 of MTCs towards the underlying substrate (i.e. the steeper slope angle, the higher the
453 momentum, and *vice versa* (Algar et al., 2011); (ii) the thickness of the overlying MTC (i.e. BSZ
454 thickness is proportional to the thickness of the overlying MTCs; e.g., MTC 3 is thicker than
455 MTC2, and thus the thickness of BSZ of the former is thicker than that of the latter; (iii) MTC
456 content; the MTCs with fewer blocks (i.e. MTC 2 and 3) will have a thicker BSZs than the MTCs
457 with more transported blocks (MTC 1); (iv) the lithology of the substrate; i.e. a ductile,
458 mudstone-rich substrate may be highly sheared, with the shear stress from the overlying
459 MTCs leading to dewatering rather than erosion of the BSZ (Alves and Lourenço, 2010; Ortiz-
460 Karpf et al., 2017); and (v) bathymetric confinement, which would influence the substrate
461 geometry, heterogeneity, internal characteristics and pathway of MTCs; the thickness of
462 MTCs and their BSZ would thus vary laterally (Ortiz-Karpf et al., 2017).

463 In detail, we suggest the inferred high shear strain characterising the BSZs can be captured in
464 a three-stage, MTC emplacement model (Figure 14a, b): (i) Phase 1 – high shear stresses
465 within the BSZs cause an increase in fluid pressure beneath the rapidly deposited very fine-
466 grained upper part of the flow; this drives liquefaction within the BSZ (Figure 14c); (ii) Phase
467 2 – continued shearing drives fluidization and pore fluid expulsion (Figure 14d); and (iii) Phase
468 3 - as gravity induced shear stress progresses, fluid escape continues, resulting in pore space
469 reduction and BSZ compaction (Figure 14e). A key observation is that, even where 30 m (98

470 ft) thick, the BSZs are too thin to be recognised in seismic reflection data (i.e. these intervals
471 are sub-seismic).

472 *Identifying MTCs using petrophysical data*

473 On the middle to lower slope of the Mississippi Fan, GR log data cannot differentiate between
474 MTCs and undeformed background deposits because both are mudstone-rich (i.e. both are
475 characterised by serrated, overall high-GR responses). In this situation, Vp and RT logs may
476 be more useful, as they may present higher values in the MTC debritic matrix than the
477 background deposits, principally because these deposits have undergone some degree of
478 transport, and thus emplacement-related strain and compaction. Our method, which may
479 allow well-based, petrophysically driven mapping of MTCs and their BSZs, can be used in
480 lower-quality 3D seismic datasets that image deep-water sedimentary successions (e.g. sub-
481 salt-canopy minibasins within which seismic resolution is relatively low).

482 7.3 Petroleum implication of MTCs

483 *MTCs as hydrocarbon seals*

484 Most petrophysics-based studies of MTCs indicate these deposits are dominated by
485 mudstone. Furthermore, these studies suggest that, because they are over-compacted, these
486 mudstone-rich MTCs may be better seals than surrounding deposits (Algar et al., 2011). This
487 study suggests that emplacement-related over-compaction in MTCs occurs within the BSZ,
488 meaning this interval may have higher sealing potential than lithologically similar background
489 deposits occurring at similar burial depths. The highly reflective nature of the BSZ of an MTC,
490 which relates to its higher density and acoustic velocity, may thus be an indicator of higher
491 sealing potential. The mudstone-rich debrite in the upper part of MTC 1 appears to be a good
492 top and lateral seal for the underlying folded and faulted sandstone-rich transported blocks

493 (Figure 4C, 4D). In MTC 2, the mudstone-rich debrite (MTC 2.1 and MTC 2.2) and the
494 corresponding BSZ may act as a good top and lateral seal for the underlying, sandstone-rich
495 parts of the remnant block (Figure 6C, 6D). In the BSZ of MTC 3, which appears to be the most
496 consolidated of all the recognised BSZs, could act as good base seal for underlying sandstone-
497 rich deposits.

498 *Reservoir potential*

499 In this study, we show that sandstone-rich transported blocks can be up to c. 180 m (590 ft)
500 thick, 6800 m (22309 ft) long, cover 2.5 km² (0.95 mi²) in map-view, and have an approximate
501 volume of 4.5 km³/1.1 mi³ (i.e. MTC 1). The sandstone-rich parts within remnant blocks
502 underlying MTC 2 are up to 20 m (65 ft) thick, cover 0.0145 km² (0.006 mi²) in map-view, and
503 have an approximate volume of 0.29 km³ (0.07 mi³). Petrophysical data indicate the
504 sandstone-rich blocks within MTC 1 and in the remnant block might be under-pressured and
505 may thus be characterised by relatively high porosities. These transported yet less-deformed
506 sandstone-rich blocks (i.e. MTC 1), and the sandstone-rich parts within the remnant blocks
507 under MTC 2, could be potential reservoirs and may thus be of interest to the hydrocarbon
508 industry (Moore et al., 1995; Alves, 2010; Dunlap et al., 2010; Principaud et al., 2015). In
509 addition and as stated above, the sandstone-rich parts within MTC 1 and the remnant blocks
510 are capped by the overlying mudstone-rich deposit, and are externally sealed by the
511 surrounding, mudstone-rich background strata. Intra-MTC blocks of comparable size to
512 those described here (i.e. 1-10 km/0.6-6 mi long, 0.3-2 km/0.18-1.2 mi wide, 50-500 m/164-
513 1640 ft thick, and covering an area of 3.63-4 km²/1.4-1.5 mi²) have been described by other
514 workers (e.g., Moscardelli et al., 2006; Ogiesoba and Hammes, 2012).

515 *Drilling hazards*

516 Typically, MTCs are more consolidated than surrounding sediments and could slow down the
517 penetration rate (i.e. Shipp, 2004). Therefore, MTCs are a major concern when designing
518 suction anchor piles and jetted conductors (Newlin, 2003). In this study, the identification of
519 the most consolidated BSZs from petrophysical data of MTCs could provide information for
520 the design of the jetted conductors and suction anchor pile. Neglecting the presence of BSZs
521 might cause unexpected problems during the penetration of MTCs (i.e. increase drilling time
522 and costly rig). In addition, we use the amplitude attribute to infer the petrophysical
523 properties of MTCs. The high amplitude nature of BSZs of MTCs could provide information on
524 identification the most consolidated section of MTCs.

525 8. Conclusions

526 We use seismic reflection and well-log data to study the seismic and petrophysical expression,
527 and lithology of three MTCs preserved in a deep-water minibasin, northern Gulf of Mexico.
528 We show that: (i) MTCs are dominated by chaotic, medium-to-low amplitude seismic
529 reflections (debrite), and packages of deformed, but more continuous, medium-to-high
530 amplitude reflections (remnant and transported blocks); (ii) MTCs are mudstone-dominated,
531 whereas the transported and remnant blocks are relatively sandstone-rich; (iii) MTCs are
532 characterised by high acoustic velocities (as revealed by Vp data) and are relatively more
533 resistive relative to surrounding background sediments at similar burial depths; (iv) the top
534 surface of the MTCs are characterised by a positive seismic reflection and the base shear
535 surface (BSS) is characterised by a negative seismic reflection; (v) the lowermost 15-30 m (49-
536 98 ft) of the MTCs define basal shear zones, which are characterised by relatively high P-wave
537 velocity (Vp) and resistivity (RT) values due to shear-induced over-compaction; (v) Vp and RT
538 vary laterally within the BSZs, being higher below the thicker, main body of MTC than towards

539 the lateral margins; (vi) the hydrocarbon seal potential of MTCs may be internally highly
540 variable, with the BSZ displaying the greatest seal capacity (smallest pore throat diameter and
541 lowest permeability) below the main body of the MTCs compared to the deposit margins; and
542 (vii) sandstone-rich blocks within the MTC 1 tend to be under-compacted and may maintain
543 anomalously high porosities. Sandstone-rich blocks also tend to be internally sealed by
544 overlying mudstone-rich debris and externally sealed by background mudstone-rich deposits.

545

546

547

548 Reference

- 549 Algar, S., C. Milton, H. Upshall, J. Roestenburg, and P. Crevello, 2011, Mass-transport deposits of the
550 deepwater northwestern Borneo margin (Malaysia)—Characterization from seismic-
551 reflection, borehole, and core data with implications for hydrocarbon exploration and
552 exploitation: Mass-transport deposits in deepwater settings: Tulsa, Oklahoma, SEPM Special
553 Publication, v. 96, p. 351-366.
- 554 Alves, T. M., 2010, 3D seismic examples of differential compaction in mass-transport deposits and
555 their effect on post-failure strata: *Marine Geology*, v. 271, p. 212-224.
- 556 Alves, T. M., 2015, Submarine slide blocks and associated soft-sediment deformation in deep-water
557 basins: a review: *Marine and Petroleum Geology*, v. 67, p. 262-285.
- 558 Alves, T. M., K. Kurtev, G. F. Moore, and M. Strasser, 2014, Assessing the internal character, reservoir
559 potential, and seal competence of mass-transport deposits using seismic texture: A
560 geophysical and petrophysical approach: *AAPG bulletin*, v. 98, p. 793-824.
- 561 Alves, T. M., and S. D. Lourenço, 2010, Geomorphologic features related to gravitational collapse:
562 Submarine landsliding to lateral spreading on a late Miocene–Quaternary slope (SE Crete,
563 eastern Mediterranean): *Geomorphology*, v. 123, p. 13-33.
- 564 Brown, A. R., 2011, Interpretation of three-dimensional seismic data, *Society of Exploration
565 Geophysicists and American Association of Petroleum Geologists*.
- 566 Bull, S., J. Cartwright, and M. Huuse, 2009, A review of kinematic indicators from mass-transport
567 complexes using 3D seismic data: *Marine and Petroleum Geology*, v. 26, p. 1132-1151.
- 568 Butler, R. W., J. T. Eggenhuisen, P. Haughton, and W. D. McCaffrey, 2016, Interpreting syndepositional
569 sediment remobilization and deformation beneath submarine gravity flows; a kinematic
570 boundary layer approach: *Journal of the Geological Society*, v. 173, p. 46-58.
- 571 Chopra, S., and K. J. Marfurt, 2007, Seismic attributes for prospect identification and reservoir
572 characterization, *Society of Exploration Geophysicists and European Association of
573 Geoscientists and Engineers*.
- 574 Doughty-Jones, G., M. Mayall, and L. Lonergan, 2017, Stratigraphy, facies, and evolution of deep-water
575 lobe complexes within a salt-controlled intraslope minibasin: *AAPG Bulletin*, v. 101, p. 1879-
576 1904.

577 Dugan, B., 2012, Petrophysical and consolidation behavior of mass transport deposits from the
578 northern Gulf of Mexico, IODP Expedition 308: Marine Geology, v. 315, p. 98-107.

579 Dugan, B., and J. T. Germaine, 2008, Near - seafloor overpressure in the deepwater Mississippi
580 Canyon, northern Gulf of Mexico: Geophysical Research Letters, v. 35.

581 Dunlap, D. B., L. J. Wood, C. Weisenberger, and H. Jabour, 2010, Seismic geomorphology of offshore
582 Moroccos east margin, Safi Haute Mer area: AAPG bulletin, v. 94, p. 615-642.

583 Dykstra, M., K. Garyfalou, V. Kertznus, B. Kneller, J. Milana, M. Molinaro, M. Szuman, and P. Thompson,
584 2011, Mass-transport deposits: combining outcrop studies and seismic forward modeling to
585 understand lithofacies distributions, deformation, and their seismic expression: Mass-
586 Transport Deposits. SEPM, Tulsa, OK.

587 Flemings, P., H. Long, B. Dugan, J. Germaine, C. John, J. H. Behrmann, D. Sawyer, and I. Expedition,
588 2008, Pore pressure penetrometers document high overpressure near the seafloor where
589 multiple submarine landslides have occurred on the continental slope, offshore Louisiana,
590 Gulf of Mexico: Earth and Planetary Science Letters, v. 269, p. 309-325.

591 Flemings, P. B., I. Behrmann, T. Davies, C. John, and E. Team, 2005, Gulf of Mexico hydrogeology—
592 Overpressure and fluid flow processes in the deepwater Gulf of Mexico: Slope stability, seeps,
593 and shallow-water flow: Integrated Ocean Drilling Program Scientific Prospectus, v. 308, p. 1-
594 52.

595 Flemings, P. B., C. John, and J. Behrmann, 2012, Expedition 308 synthesis: overpressure, consolidation,
596 and slope stability on the continental slope of the Gulf of Mexico.

597 Frey Martinez, J., J. Cartwright, and B. Hall, 2005, 3D seismic interpretation of slump complexes:
598 examples from the continental margin of Israel: Basin Research, v. 17, p. 83-108.

599 Galloway, W. E., 2001, Cenozoic evolution of sediment accumulation in deltaic and shore-zone
600 depositional systems, northern Gulf of Mexico Basin: Marine and Petroleum Geology, v. 18, p.
601 1031-1040.

602 Galloway, W. E., 2008, Depositional evolution of the Gulf of Mexico sedimentary basin: Sedimentary
603 basins of the world, v. 5, p. 505-549.

604 Galloway, W. E., P. E. Ganey-Curry, X. Li, and R. T. Buffler, 2000, Cenozoic depositional history of the
605 Gulf of Mexico basin: AAPG bulletin, v. 84, p. 1743-1774.

606 Galloway, W. E., T. L. Whiteaker, and P. Ganey-Curry, 2011, History of Cenozoic North American
607 drainage basin evolution, sediment yield, and accumulation in the Gulf of Mexico basin:
608 Geosphere, v. 7, p. 938-973.

609 Hodgson, D., H. Brooks, A. Ortiz-Karppf, Y. Spychala, D. Lee, and C.-L. Jackson, 2018, Entrainment and
610 abrasion of megaclasts during submarine landsliding and their impact on flow behaviour:
611 Geological Society, London, Special Publications, v. 477, p. SP477. 26.

612 Hühnerbach, V., and D. Masson, 2004, Landslides in the North Atlantic and its adjacent seas: an
613 analysis of their morphology, setting and behaviour: Marine Geology, v. 213, p. 343-362.

614 Jackson, C. A.-L., Y. Zhang, D. A. Herron, and P. J. Fitch, 2018, Subsurface expression of a tertiary salt
615 weld, Gulf of Mexico: Petroleum Geoscience, p. petgeo2018-008.

616 Jackson, C. A., and H. D. Johnson, 2009, Sustained turbidity currents and their interaction with debrite-
617 related topography; Labuan Island, offshore NW Borneo, Malaysia: Sedimentary Geology, v.
618 219, p. 77-96.

619 King, P. R., B. R. Ilg, M. Arnot, G. H. Browne, L. J. Strachan, M. Crundwell, K. Helle, R. Shipp, P. Weimer,
620 and H. Posamentier, 2011, Outcrop and seismic examples of mass-transport deposits from a
621 late Miocene deep-water succession, Taranaki Basin, New Zealand: Mass-transport deposits
622 in deepwater settings: Society for Sedimentary Geology (SEPM) Special Publication 96, p. 311-
623 347.

624 Kneller, B., M. Dykstra, L. Fairweather, and J. P. Milana, 2016, Mass-transport and slope
625 accommodation: implications for turbidite sandstone reservoirs: AAPG Bulletin, v. 100, p. 213-
626 235.

627 Koson, S., P. Chenrai, and M. Choowong, 2014, Seismic attributes and their applications in seismic
628 geomorphology: *Bulletin of Earth Sciences of Thailand*, v. 6, p. 1-9.

629 Lee, H. J., J. Locat, P. Desgagnés, J. D. Parsons, B. G. McAdoo, D. L. Orange, P. Puig, F. L. Wong, P.
630 Dartnell, and E. Boulanger, 2007, Submarine mass movements on continental margins,
631 Continental margin sedimentation: from sediment transport to sequence stratigraphy, v. 37,
632 *Citeaser*, p. 213-274.

633 Long, H., P. Flemings, J. Germaine, and D. Saffer, 2011, Consolidation and overpressure near the
634 seafloor in the Ursa Basin, Deepwater Gulf of Mexico: *Earth and Planetary Science Letters*, v.
635 305, p. 11-20.

636 Madof, A. S., N. Christie-Blick, and M. H. Anders, 2009, Stratigraphic controls on a salt-withdrawal
637 intraslope minibasin, north-central Green Canyon, Gulf of Mexico: Implications for
638 misinterpreting sea level change: *AAPG bulletin*, v. 93, p. 535-561.

639 Mahaffie, M., 1995, Reservoir classification for turbidite intervals at the Mars discovery, Mississippi
640 Canyon Block 807, Gulf of Mexico.

641 Major, J. J., and R. M. Iverson, 1999, Debris-flow deposition: Effects of pore-fluid pressure and friction
642 concentrated at flow margins: *Geological Society of America Bulletin*, v. 111, p. 1424-1434.

643 Martin, R. G., and A. H. Bouma, 1982, Active diapirism and slope steepening, northern Gulf of Mexico
644 continental slope: *Marine Georesources & Geotechnology*, v. 5, p. 63-91.

645 Martinsen, O., 1989, Styles of soft-sediment deformation on a Namurian (Carboniferous) delta slope,
646 Western Irish Namurian Basin, Ireland: *Geological Society, London, Special Publications*, v. 41,
647 p. 167-177.

648 Martinsen, O. J., T. Lien, R. G. Walker, and J. D. Collinson, 2003, Facies and sequential organisation of
649 a mudstone-dominated slope and basin floor succession: the Gull Island Formation, Shannon
650 Basin, Western Ireland: *Marine and Petroleum Geology*, v. 20, p. 789-807.

651 Meckel III, L., 2011, Reservoir characteristics and classification of sand-prone submarine mass-
652 transport deposits: *SEPM Special Publication*, v. 96, p. 432-452.

653 Meissl, S., J. Behrmann, and J. H. Behrmann, 2010, Data report: preliminary assessment of Pleistocene
654 sediment strength in the Ursa Basin (Gulf of Mexico continental slope) from triaxial and ring
655 shear test data: *Proceedings of the Integrated Ocean Drilling Program*.

656 Moernaut, J., and M. De Batist, 2011, Frontal emplacement and mobility of sublacustrine landslides:
657 results from morphometric and seismostratigraphic analysis: *Marine Geology*, v. 285, p. 29-
658 45.

659 Moore, J. G., W. B. Bryan, M. H. Beeson, and W. R. Normark, 1995, Giant blocks in the South Kona
660 landslide, Hawaii: *Geology*, v. 23, p. 125-128.

661 Moscardelli, L., and L. Wood, 2008, New classification system for mass transport complexes in offshore
662 Trinidad: *Basin Research*, v. 20, p. 73-98.

663 Moscardelli, L., L. Wood, and P. Mann, 2006, Mass-transport complexes and associated processes in
664 the offshore area of Trinidad and Venezuela: *AAPG bulletin*, v. 90, p. 1059-1088.

665 Newlin, J., 2003, Suction Anchor Piles for the Na Kika FDS Mooring System Part 2: Installation
666 Performance, *Deepwater mooring systems: Concepts, design, analysis, and materials*, p. 55-
667 75.

668 Ogata, K., J. Mountjoy, G. A. Pini, A. Festa, and R. Tinterri, 2014, Shear zone liquefaction in mass
669 transport deposit emplacement: A multi-scale integration of seismic reflection and outcrop
670 data: *Marine Geology*, v. 356, p. 50-64.

671 Ogiesoba, O., and U. Hammes, 2012, Seismic interpretation of mass-transport deposits within the
672 upper Oligocene Frio Formation, south Texas Gulf Coast: *AAPG bulletin*, v. 96, p. 845-868.

673 Ortiz-Karpp, A., D. Hodgson, and W. McCaffrey, 2015, The role of mass-transport complexes in
674 controlling channel avulsion and the subsequent sediment dispersal patterns on an active
675 margin: the Magdalena Fan, offshore Colombia: *Marine and Petroleum Geology*, v. 64, p. 58-
676 75.

677 Ortiz-Karpf, A., D. M. Hodgson, C. A.-L. Jackson, and W. D. McCaffrey, 2017, Influence of Seabed
678 Morphology and Substrate Composition On Mass-Transport Flow Processes and Pathways:
679 Insights From the Magdalena Fan, Offshore Colombia: *Journal of Sedimentary Research*, v. 87,
680 p. 189-209.

681 Ortiz - Karpf, A., D. M. Hodgson, C. A. L. Jackson, and W. D. McCaffrey, 2016, Mass - Transport
682 Complexes as Markers of Deep - Water Fold - and - Thrust Belt Evolution: Insights from the
683 Southern Magdalena Fan, Offshore Colombia: *Basin Research*.

684 Peel, F., C. Travis, and J. Hossack, 1995, Genetic structural provinces and salt tectonics of the Cenozoic
685 offshore US Gulf of Mexico: A preliminary analysis.

686 Perov, G., and J. P. Bhattacharya, 2011, Pleistocene shelf-margin delta: Intradeltaic deformation and
687 sediment bypass, northern Gulf of Mexico: *AAPG bulletin*, v. 95, p. 1617-1641.

688 Pickering, K., and R. Hiscott, 2015, *Deep Marine Systems: Processes, Deposits, Environments, Tectonic
689 and Sedimentation*, John Wiley & Sons.

690 Piper, D., C. Pirmez, P. Manley, D. Long, R. Flood, W. Normark, and W. Showers, 1997, Mass-transport
691 deposits of the Amazon Fan: *PROCEEDINGS-OCEAN DRILLING PROGRAM SCIENTIFIC RESULTS*,
692 p. 109-146.

693 Posamentier, H. W., 2005, Stratigraphy and geomorphology of deep-water mass transport complexes
694 based on 3D seismic data, *SEG Technical Program Expanded Abstracts 2005*, Society of
695 Exploration Geophysicists, p. 2300-2303.

696 Posamentier, H. W., and V. Kolla, 2003, Seismic geomorphology and stratigraphy of depositional
697 elements in deep-water settings: *Journal of sedimentary research*, v. 73, p. 367-388.

698 Posamentier, H. W., and O. J. Martinsen, 2011, The character and genesis of submarine mass-transport
699 deposits: insights from outcrop and 3D seismic data: *Mass-transport deposits in deepwater
700 settings: Society for Sedimentary Geology (SEPM) Special Publication 96*, p. 7-38.

701 Prather, B. E., J. R. Booth, G. S. Steffens, and P. A. Craig, 1998, Classification, lithologic calibration, and
702 stratigraphic succession of seismic facies of intraslope basins, deep-water Gulf of Mexico:
703 *AAPG bulletin*, v. 82, p. 701-728.

704 Principaud, M., T. Mulder, H. Gillet, and J. Borgomano, 2015, Large-scale carbonate submarine mass-
705 wasting along the northwestern slope of the Great Bahama Bank (Bahamas): Morphology,
706 architecture, and mechanisms: *Sedimentary Geology*, v. 317, p. 27-42.

707 Roesink, J. G., P. Weimer, and R. Bouroulllec, 2004, Sequence stratigraphy of Miocene to Pleistocene
708 sediments of east-central Mississippi canyon, northern Gulf of Mexico.

709 Sassa, S., J. Miyamoto, and H. Sekiguchi, 2003, The dynamics of liquefied sediment flow undergoing
710 progressive solidification, *Submarine Mass Movements and Their Consequences*, Springer, p.
711 95-102.

712 Saucier, R. T., 1997, *Geomorphology and Quarternary Geologic History of the Lower Mississippi Valley*.
713 Volume 1.

714 Sawyer, D. E., 2007, Lateral Variations in Core, Log, and Seismic Attributes of a Mass Transport
715 Complex in the Ursa Region, IODP Expedition 308, Northern Gulf of Mexico.

716 Sawyer, D. E., P. B. Flemings, B. Dugan, and J. T. Germaine, 2009, Retrogressive failures recorded in
717 mass transport deposits in the Ursa Basin, Northern Gulf of Mexico: *Journal of Geophysical
718 Research: Solid Earth*, v. 114.

719 Sawyer, D. E., P. B. Flemings, R. C. Shipp, and C. D. Winker, 2007, Seismic geomorphology, lithology,
720 and evolution of the late Pleistocene Mars-Ursa turbidite region, Mississippi Canyon area,
721 northern Gulf of Mexico: *AAPG bulletin*, v. 91, p. 215-234.

722 Shipp, R. C., 2004, Physical Characteristics and Impact of Mass Transport Complexes on Deepwater
723 Jetted Conductors and Suction Anchor Piles.

724 Shipp, R. C., J. A. Nott, and J. A. Newlin, 2004, Physical characteristics and impact of mass transport
725 complexes on deepwater jetted conductors and suction anchor piles: *Offshore Technology
726 Conference*.

727 Shipp, R. C., P. Weimer, and H. W. Posamentier, 2011, Mass-transport deposits in deepwater settings,
728 SEPM Soc for Sed Geology.

729 Sikkema, W., and K. M. Wojcik, 2000, 3D Visualization of Turbidite Systems, Lower Congo Basin,
730 Offshore Angola, *in* P. Weimer, ed., Deep-Water Reservoirs of the World, SEPM Society for
731 Sedimentary Geology.

732 Sincavage, R., P. Weimer, and R. Bouroullec, 2004, Sequence Stratigraphy of Upper-Miocene to
733 Pleistocene Sediments of Southwestern Mississippi Canyon and Northwestern Atwater Valley,
734 Northern Gulf of Mexico.

735 Sobiesiak, M. S., B. Kneller, G. I. Alsop, and J. P. Milana, 2016, Internal deformation and kinematic
736 indicators within a tripartite mass transport deposit, NW Argentina: *Sedimentary Geology*.

737 Solheim, A., P. Bryn, H. Sejrup, J. Mienert, and K. Berg, 2005, Ormen Lange—an integrated study for
738 the safe development of a deep-water gas field within the Storegga Slide Complex, NE Atlantic
739 continental margin; executive summary, Ormen Lange—an Integrated Study for Safe Field
740 Development in the Storegga Submarine Area, Elsevier, p. 1-9.

741 Strasser, M., P. Henry, T. Kanamatsu, M. K. Thu, G. F. Moore, and I. Expedition, 2012, Scientific drilling
742 of mass-transport deposits in the Nankai accretionary wedge: First results from IODP
743 Expedition 333, Submarine mass movements and their consequences, Springer, p. 671-681.

744 Strong, H. E., 2009, The origin and properties of mass transport deposits, Ursa Basin, Gulf of Mexico.

745 Talling, P. J., D. G. Masson, E. J. Sumner, and G. Malgesini, 2012, Subaqueous sediment density flows:
746 Depositional processes and deposit types: *Sedimentology*, v. 59, p. 1937-2003.

747 Urgeles, R., and A. Camerlenghi, 2013, Submarine landslides of the Mediterranean Sea: Trigger
748 mechanisms, dynamics, and frequency - magnitude distribution: *Journal of Geophysical
749 Research: Earth Surface*, v. 118, p. 2600-2618.

750 Van Bemmell, P. P., and R. E. Pepper, 2000, Seismic signal processing method and apparatus for
751 generating a cube of variance values, Google Patents.

752 Varnes, D. J., 1978, Slope movement types and processes: Special report, v. 176, p. 11-33.

753 Weimer, P., P. Varnai, F. M. Budhijanto, Z. M. Acosta, R. E. Martinez, A. F. Navarro, M. G. Rowan, B. C.
754 McBride, T. Villamil, and C. Arango, 1998, Sequence stratigraphy of Pliocene and Pleistocene
755 turbidite systems, northern Green Canyon and Ewing Bank (offshore Louisiana), northern Gulf
756 of Mexico: *AAPG bulletin*, v. 82, p. 918-960.

757 Winker, C. D., and J. R. Booth, 2000, Sedimentary dynamics of the salt-dominated continental slope,
758 Gulf of Mexico: integration of observations from the seafloor, near-surface, and deep
759 subsurface: GCSSEPM Foundation 20th Annual Research Conference, Deep-Water Reservoirs
760 of the World, p. 1059-1086.

761

762

763

764

765

766

767

768

769

770

771
772
773
774
775
776
777
778
779

780 Figure captions

781 Figure 1. Location map of the study area and study area relative to the globe map, showing the
782 study area (red box), the position of the modern shelf edge (black dotted line), Pleistocene-
783 shelf edge (white dotted line), and modern depositional systems. The location of the
784 Pleistocene-shelf edge is inferred from Galloway et al. (2011), the Northern Gulf of Mexico
785 Deepwater Bathymetry is created by using Arcgis, the hillshade map is cited from The Bureau
786 of Ocean Energy Management (BOEM).

787 Figure 2. Seabed map along the study area and depth map for top salt (from 3D seismic data),
788 showing the overall salt-tectonic structure of the study area. 1-5 and A-C refer to minibasins
789 and salt structures, respectively, described in the text, and the contour interval is 500 m.

790 Figure 3. (A) N-S trending seismic section showing the overall salt-tectonic structure of the
791 study area. (B) The eight key seismic horizons (H0 to seabed) and main MTC-bearing intervals.
792 (C) The main seismic facies and depositional element interpretation, please note that colour
793 in the legend refers to the different types of seismic facies. See Figure 2 for the location of
794 the seismic line. Note the position of well AT-8 #1 ST.

795 Figure 4. (A) Variance attribute calculated for the interval between the H1 and H2 seismic
796 horizons. The red dot indicates the well location; A-C are salt diapirs referred to in the text.
797 (B) Sketch of MTC 1 indicating some of the key internal structures. Note: (i) the ramp; (ii) the
798 MTC lateral margin; (iii) salt-related normal faults, (iv) intra-MTC thrusts; and (v) transported
799 blocks. (C) WNW-ESE trending seismic profile showing the range of seismic facies within MTC
800 1 (see figure 4A for location). (D) ENE-WSW trending seismic profile showing the range of
801 seismic facies within MTC 1. See figure 4A for location, the definition of the polarity and AI
802 convention in Figure 3A, and the un-interpreted seismic sections in supplementary material
803 4.

804 Figure 5. (A) Wireline logs, interpreted lithology, and extracted seismic reflection of MTC 1.
805 Log tracks are gamma ray, sonic (DTCO1), resistivity (ATR1), lithology interpreted by gamma
806 ray and acoustic log. (B) V_{shale} (V_{sh}) against P-wave velocity (V_p) cross plot for three seismic
807 facies associations within MTC 1. Each seismic facies tend to plot in a distinct cluster with
808 however some dots are plotting away from correlated cluster. Note in Fig. 5A the black dashed
809 lines are top and base boundaries of MTC1, and the black dotted lines are boundaries of each
810 seismic facies. DTCO stands for Delta-Time Compressional (microsec/ft), ATR stands for
811 Attenuation resistivity (deep; ohm-m). The depth is in measured depth.

812 Figure 6. (A) Variance attribute calculated on the H2.1 seismic horizon. The red dot indicates
813 the well location; A-C are salt diapirs referred to in the text. (B) Sketch of MTC 2 indicating
814 some key structures and features. Note: (i) the remnant block, (ii) salt-related normal faults,
815 and (iii) lateral margin. (C) NNE-SSW trending seismic profile showing the range of seismic
816 facies within MTC 2 (see figure 4.1 for location). (D) WWE-ESE trending seismic profile
817 showing the range of seismic facies within MTC 2 (see figure 6A for location). The vertical axis

818 is in measured depth. See figure 6A for location, the definition of the polarity and AI
819 convention in Figure 3A, and the un-interpreted seismic sections in supplementary material
820 5.

821 Figure 7. (A) Wireline logs, interpreted lithology, and extracted seismic reflection of MTC 2.
822 Log tracks are gamma ray, sonic (DTCO1), resistivity (ATR1), lithology interpreted by gamma
823 ray and acoustic log. (B) V_{shale} (Vsh) against P-wave velocity (V_p) cross plot for three seismic
824 facies associations within MTC 2. Each seismic facies tend to plot in a distinct cluster with
825 however some dots are plotting away from correlated cluster. Note in Fig. 7A the black dashed
826 lines are top and base boundaries of MTC2, and the black dotted lines are boundaries of each
827 seismic facies. DTCO stands for Delta-Time Compressional (microsec/ft), ATR stands for
828 Attenuation resistivity (deep; ohm-m). The depth is in measured depth.

829 Figure 8. (A) Chaos attribute calculated for the interval between the H4 and H4.1 seismic
830 horizons. The red dot indicates the well location; A-C are salt diapirs referred to in the text.
831 (B) Sketch of MTC 3 indicating some key structures and features. Note: (i) the remnant block,
832 (ii) salt-related normal faults, and (iii) lateral margin. (C) WWE-trending seismic profile
833 showing the range of seismic facies within MTC 3 (see figure 8A for location). (D) WWE-
834 trending seismic profile showing the range of seismic facies within MTC 3. See figure 8A for
835 location, the definition of the polarity and AI convention in Figure 3A, and the un-interpreted
836 seismic sections in supplementary material 6.

837 Figure 9. (A) Wireline logs and interpreted lithology of MTC 3. Log tracks are gamma ray,
838 acoustic (DTCO1), resistivity (ATR1), lithology interpreted by gamma ray and acoustic log, and
839 extracted seismic reflection. Note the black dashed lines are top and bottom boundaries of
840 MTC1, black dotted lines are boundaries of each seismic facies. DTCO stands for Delta-Time

841 Compressional (microsec/ft), ATR stands for Attenuation resistivity (deep; ohm-m). (B) V_{shale}
842 against Velocity cross plot for seismic facies 3.2 associations within MTC 3. The depth is in
843 measured depth.

844 Figure 10. (A) P-wave velocity (V_p) log, interpreted lithology column, and a schematic sketch
845 of V_p depth trend. (B) Resistivity (R_t) log, interpreted lithology column and correlated seismic
846 section. Note that the dotted black line in Figure 10A indicates inferred hydrostatic trend
847 based on V_p log.

848 Figure 11. (A) Amplitude map extracted at the top surface of MTC 1 and its correlative surface
849 overlying undeformed strata. Yellowish colour occurs when MTC 1 underlies the surface, and
850 blueish colour corresponds to the surface overlying undeformed strata. (B) Amplitude map
851 extracted at basal shear surface of MTC 1 and its correlative surface underlying undeformed
852 strata. Bright amplitude occurs when MTC 1 overlays the surface, and dim amplitude
853 corresponds to the surface underlying undeformed strata. (C) Schematic cross-section of MTC
854 1 and its correlative undeformed strata, see location from Figure 11A.

855 Figure 12. (A) Velocity (V_p) and Resistivity (R_t) logs of mudstone-rich deposits covering
856 background and MTC deposits. (B) Velocity (V_p) and Resistivity (R_t) logs of sandstone-rich
857 deposits covering background and MTC deposits, and their correlated seismic section.

858 Figure 13. (A) Velocity (V_p) and Resistivity (R_t) logs of MTC 3. (B) Velocity (V_p) and Resistivity
859 (R_t) logs of MTC 2. (C) Velocity (V_p) and Resistivity (R_t) logs of MTC 1, see the depth interval
860 from Velocity (V_p) log in Figure 10.

861 Figure 14 a) Schematic sketch of MTC and its basal shear zone; b) schematic sketch of Vp and
862 RT logs within MTC intervals. Schematic sketch of processes within the basal shear zone (see
863 location in a): liquefaction (c); fluid escape (d); overcompaction (e).

864 Table captions

865 Table 1 Summary of seismic facies in minibasin 5, including well logs, lithology, schematic
866 facies geometries, facies characteristics, and depositional environment.

867 Table 2 Approximate dimensions of MTCs by log mapping. Note that the thickness of MTCs
868 indicate the maximum total thickness.

Figure 1

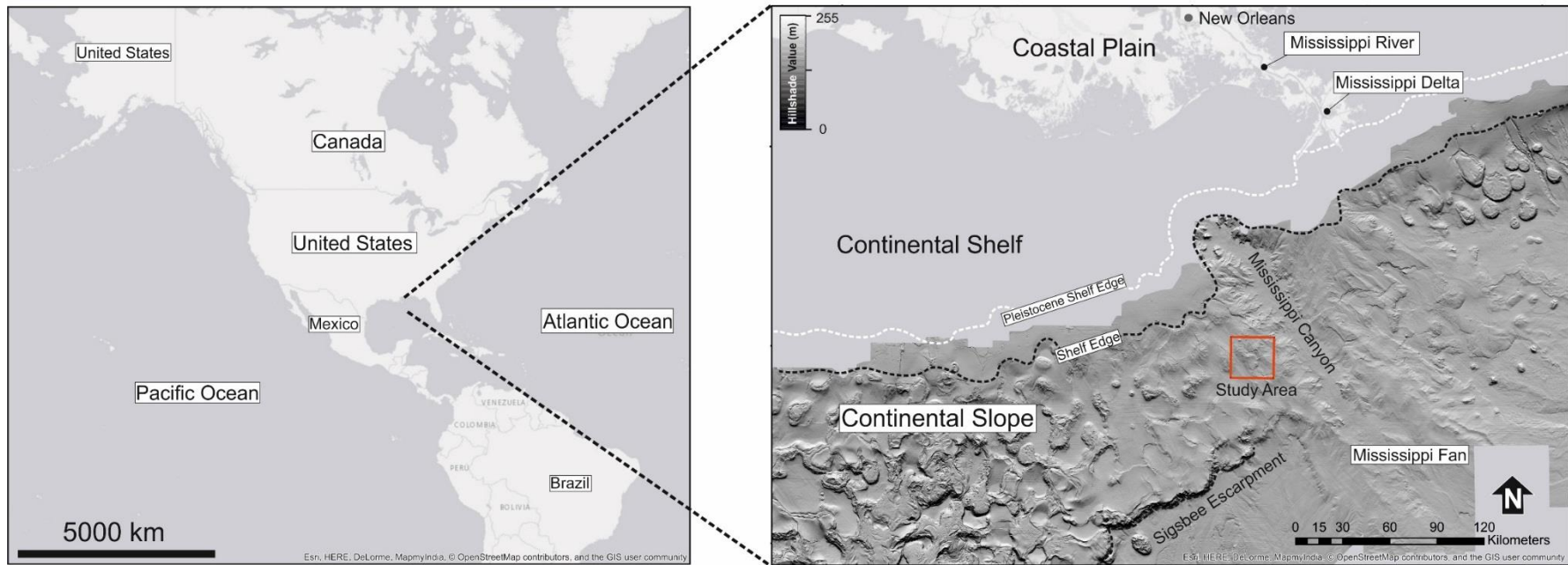


Figure 2A

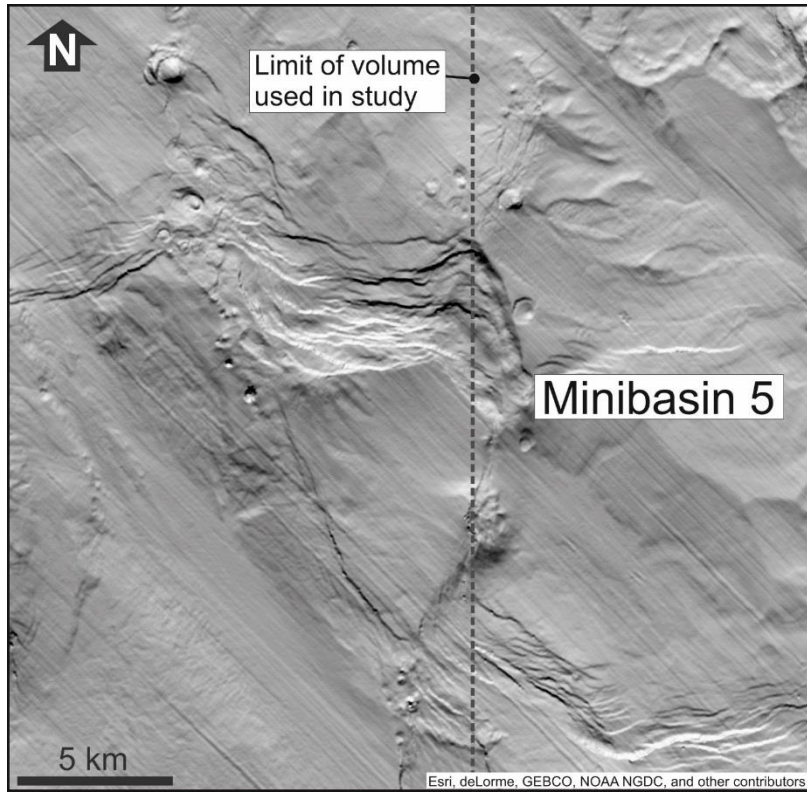


Figure 2B

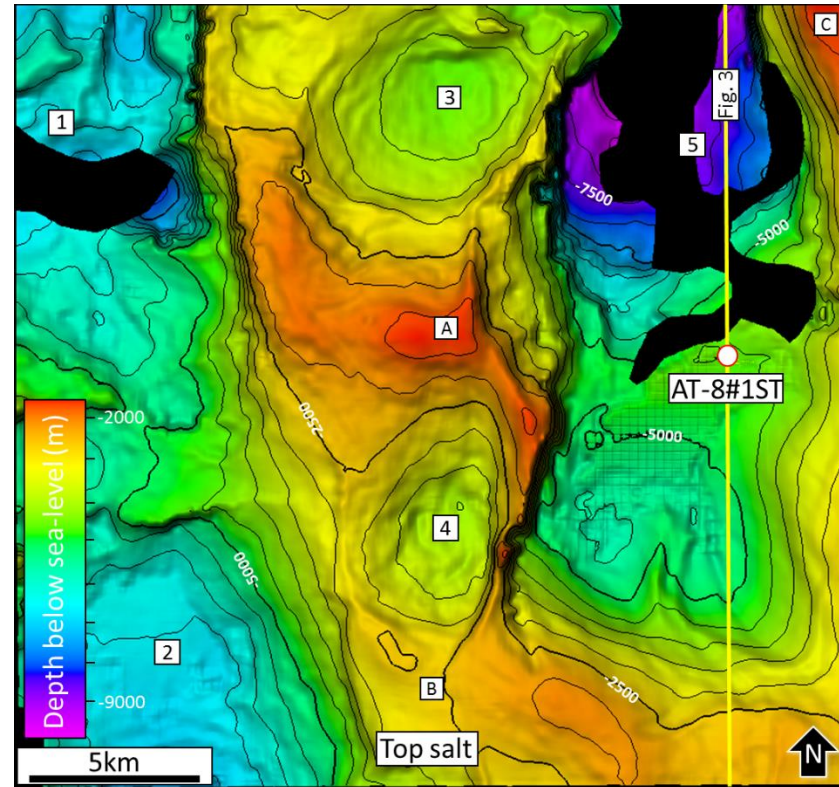


Figure 3A

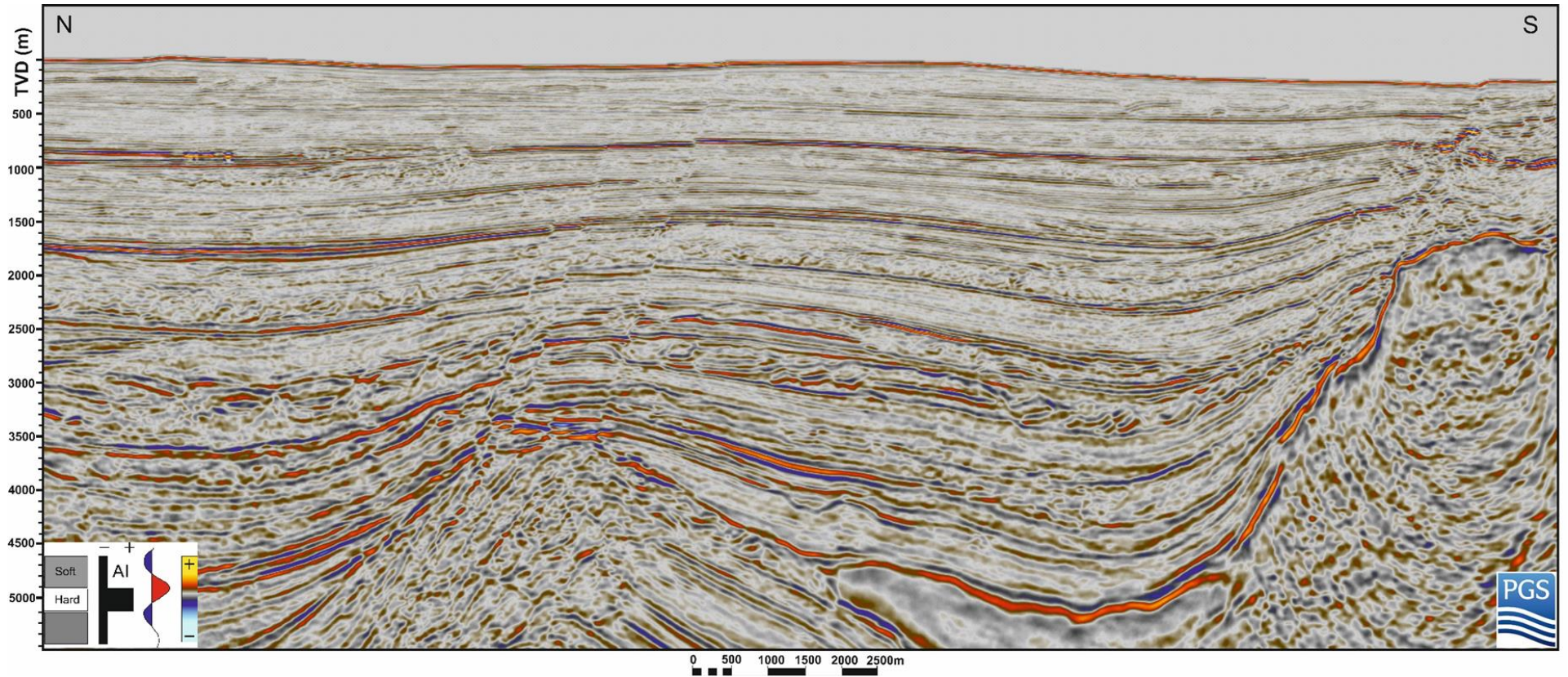


Figure 3B

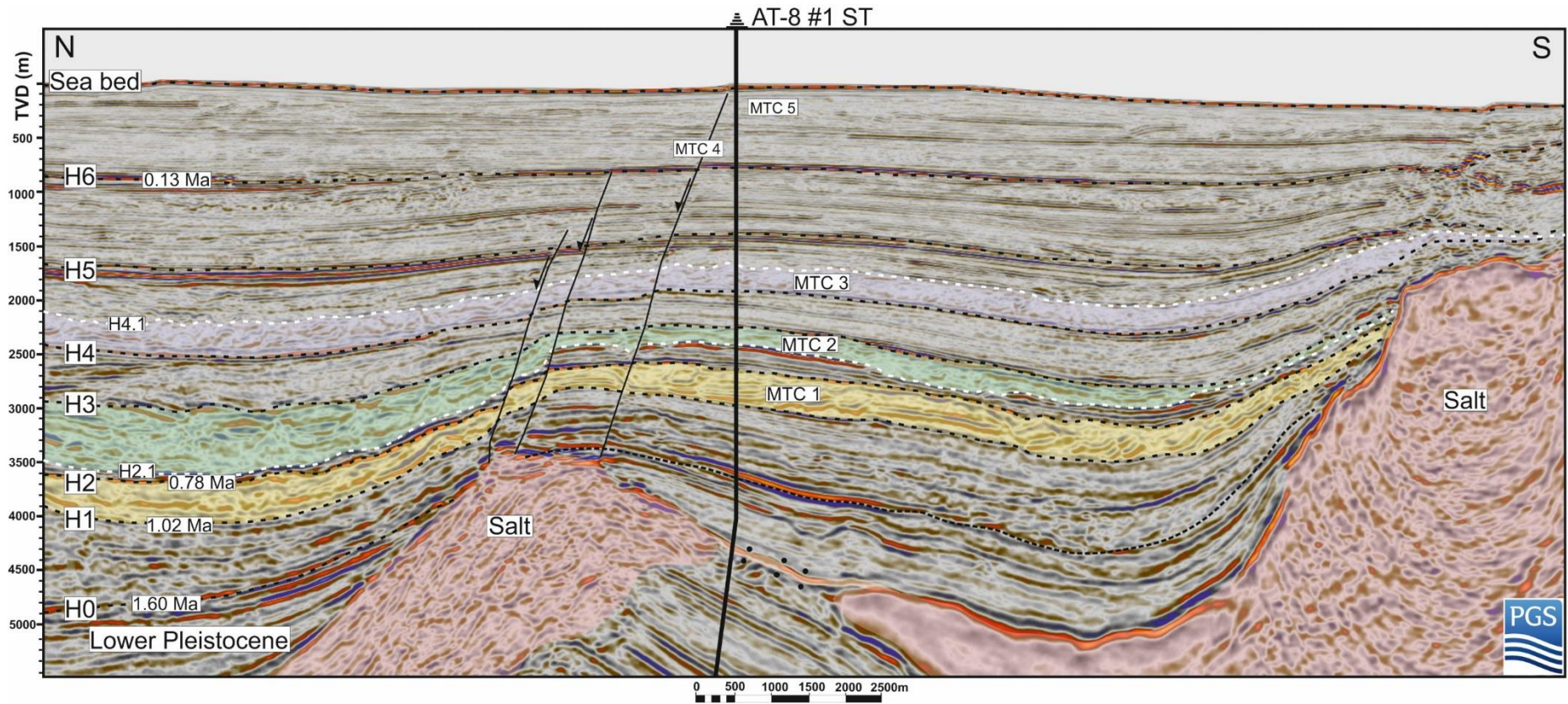


Figure 3C

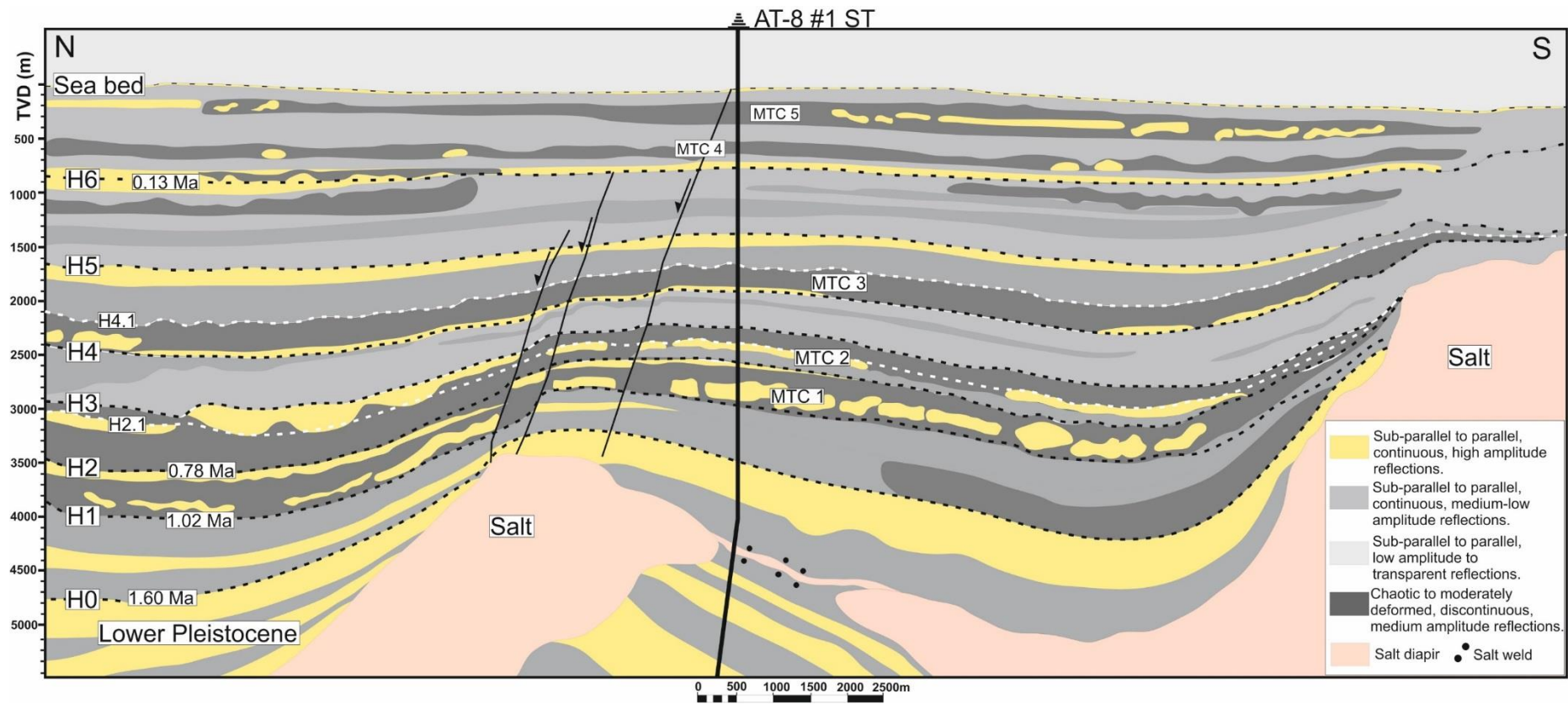


Figure 4A

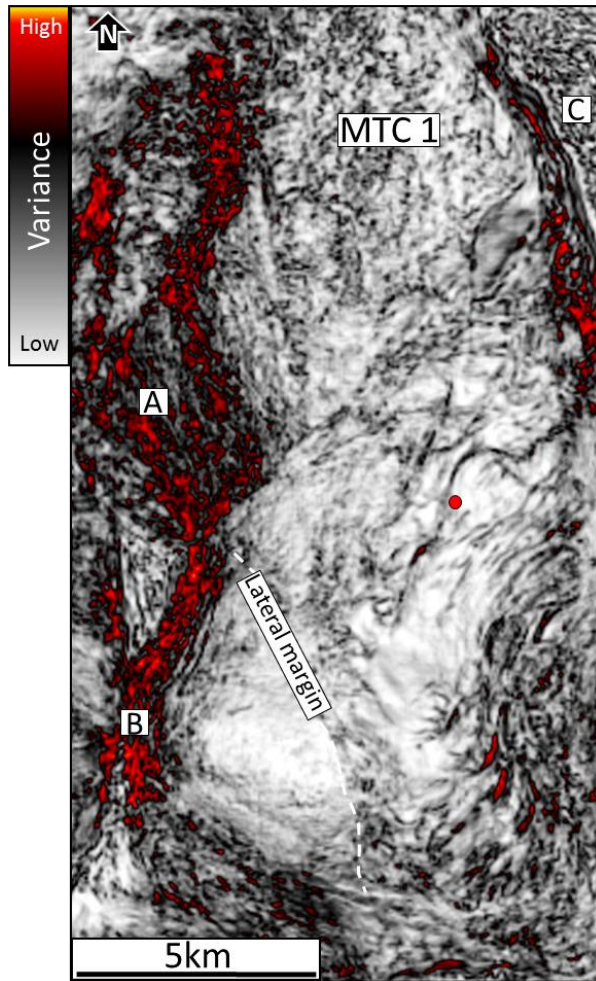


Figure 4B

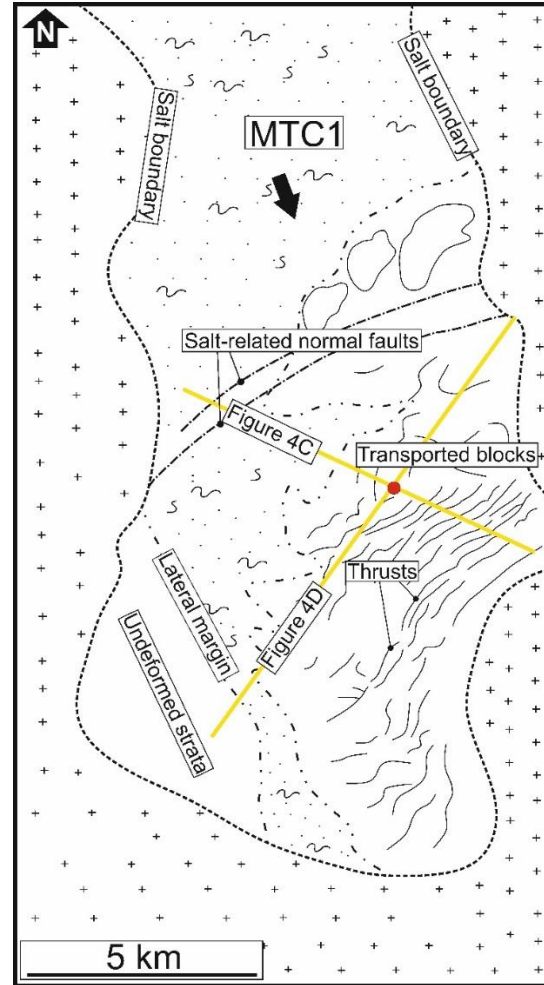


Figure 4C

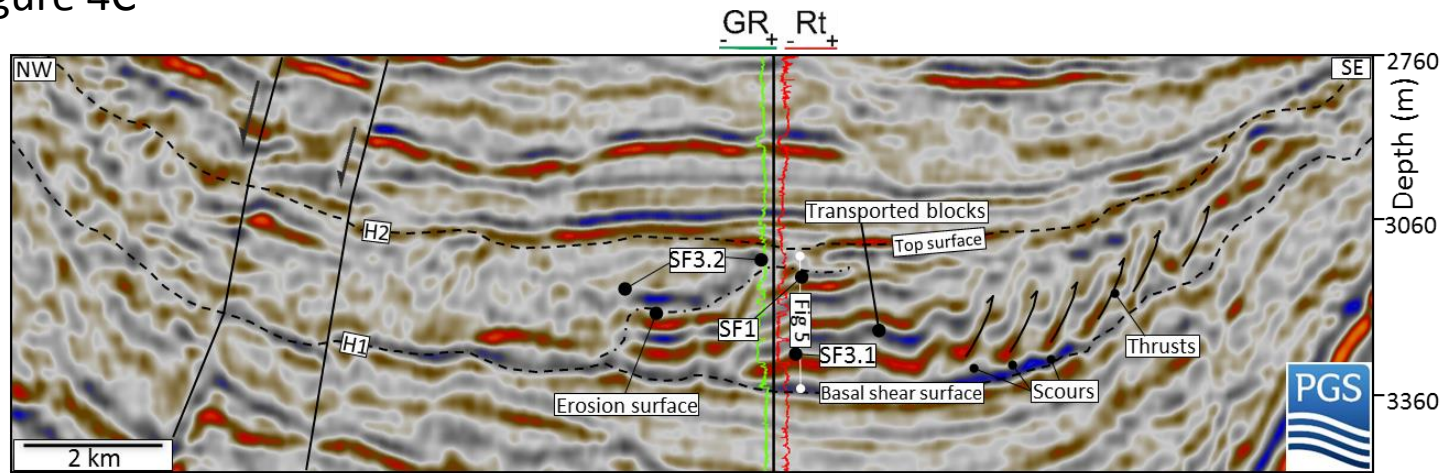


Figure 4D

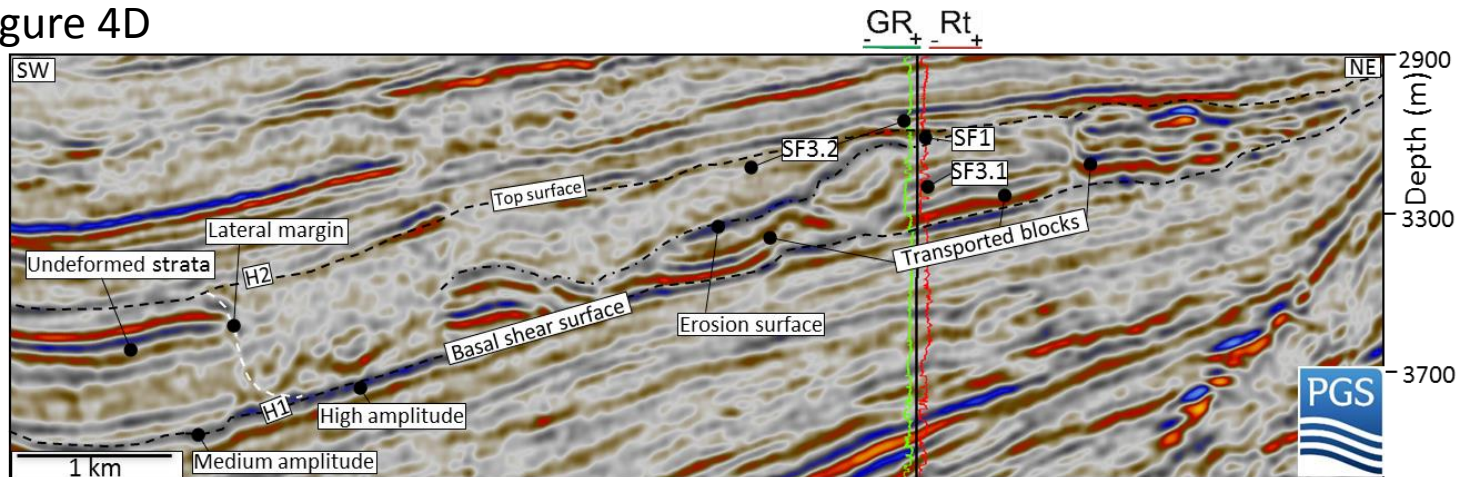


Figure 5A

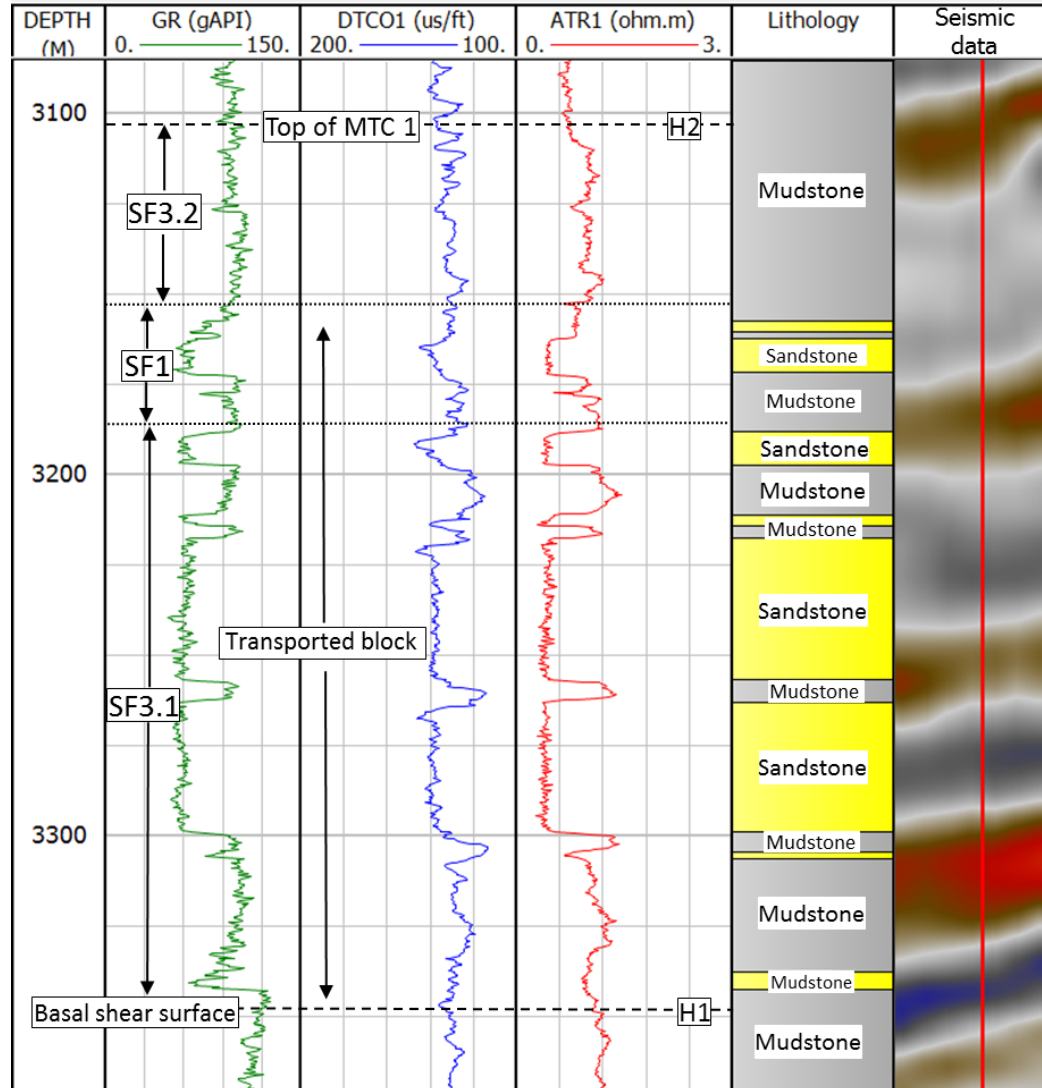


Figure 5B

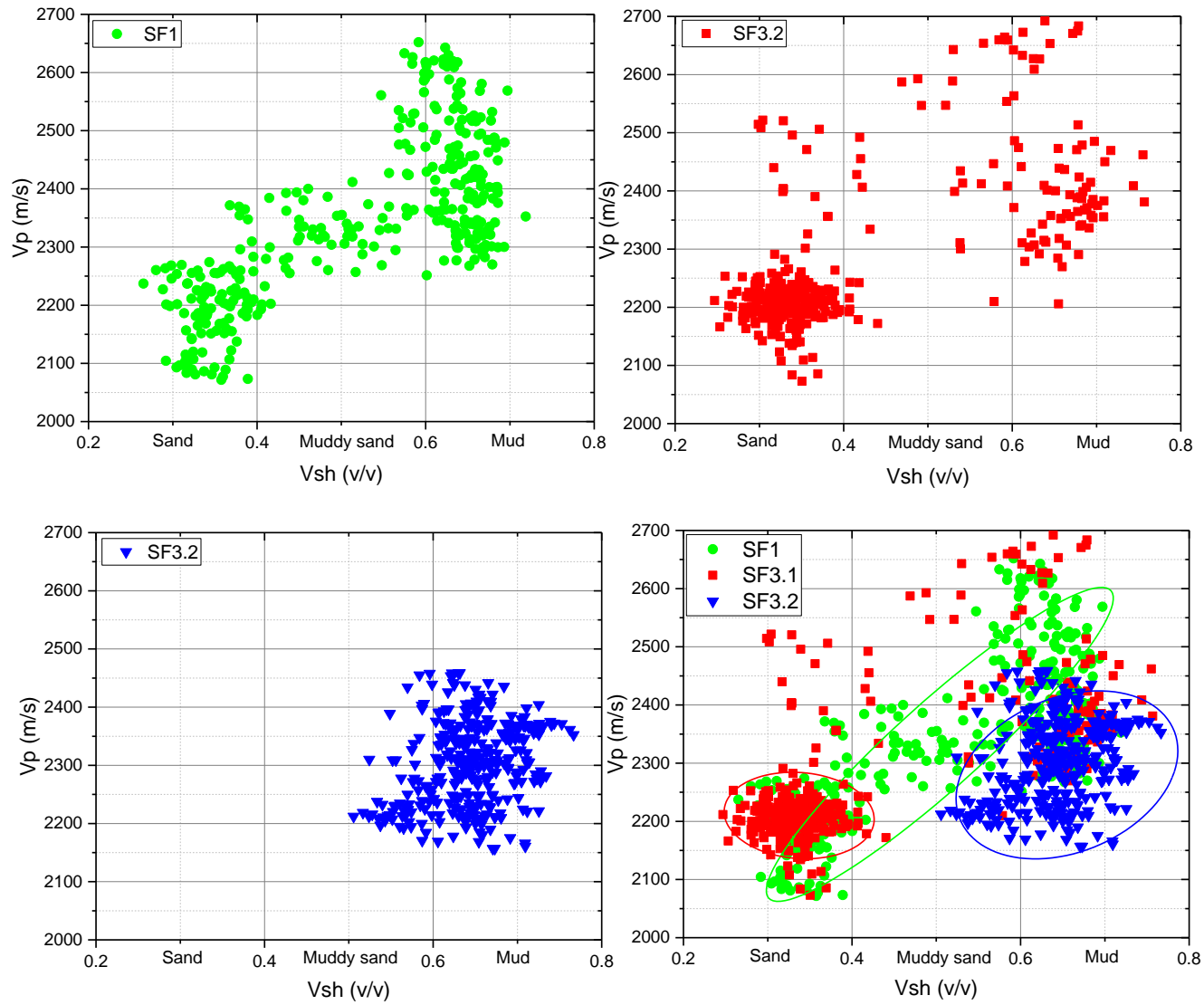


Figure 6A

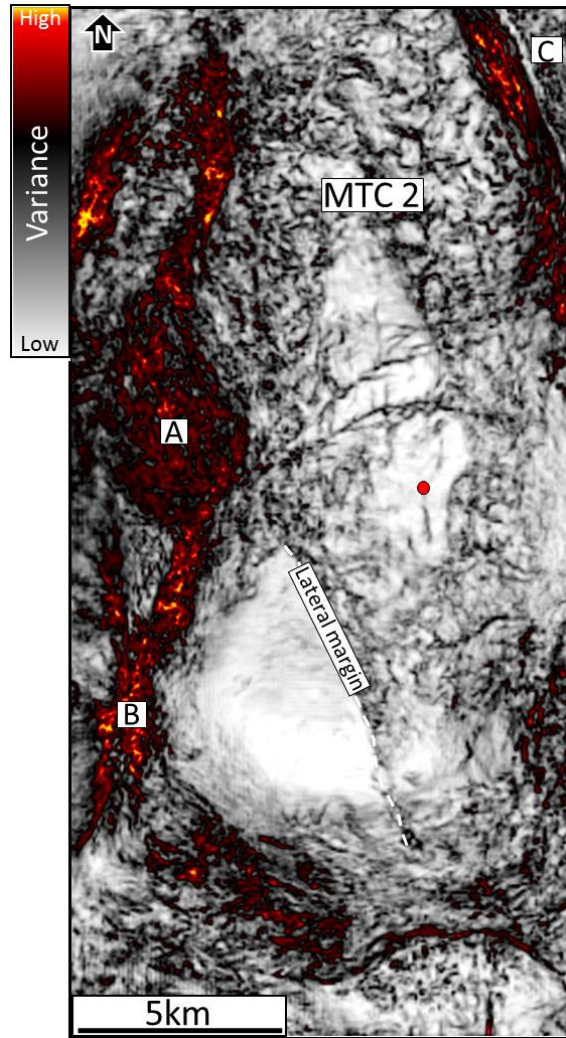


Figure 6B

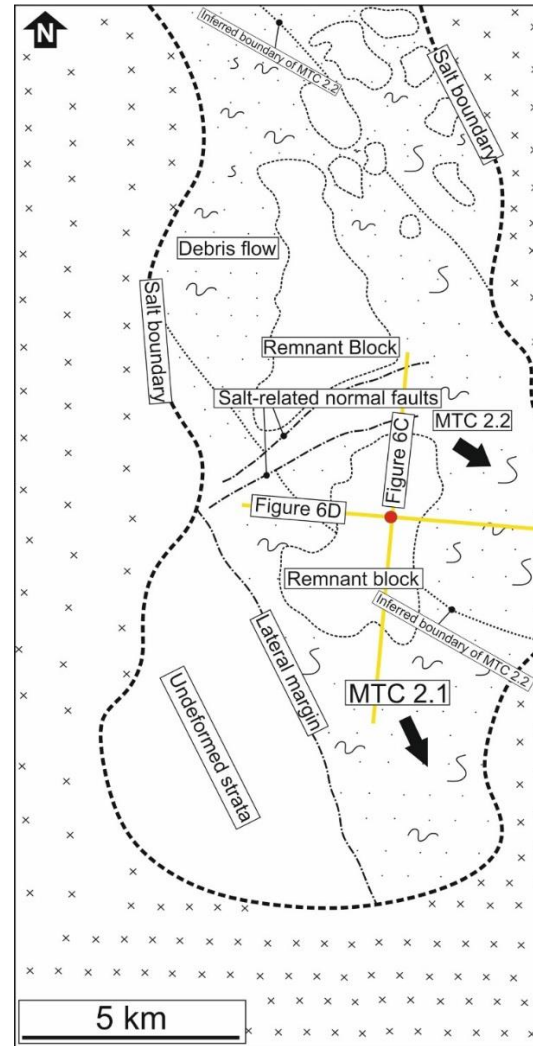


Figure 6C

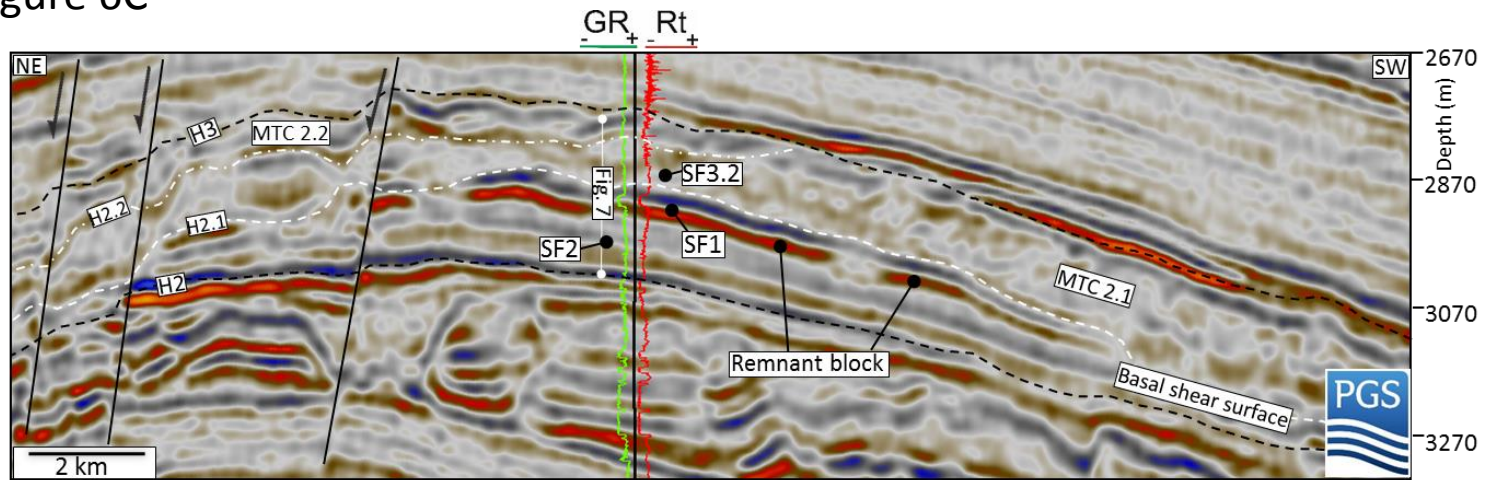


Figure 6D

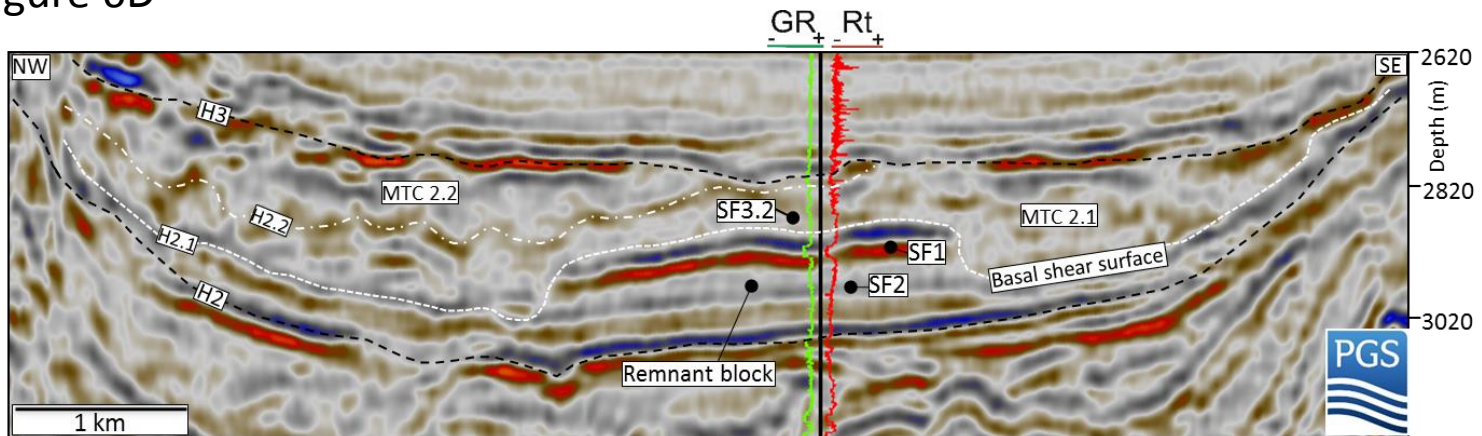


Figure 7A

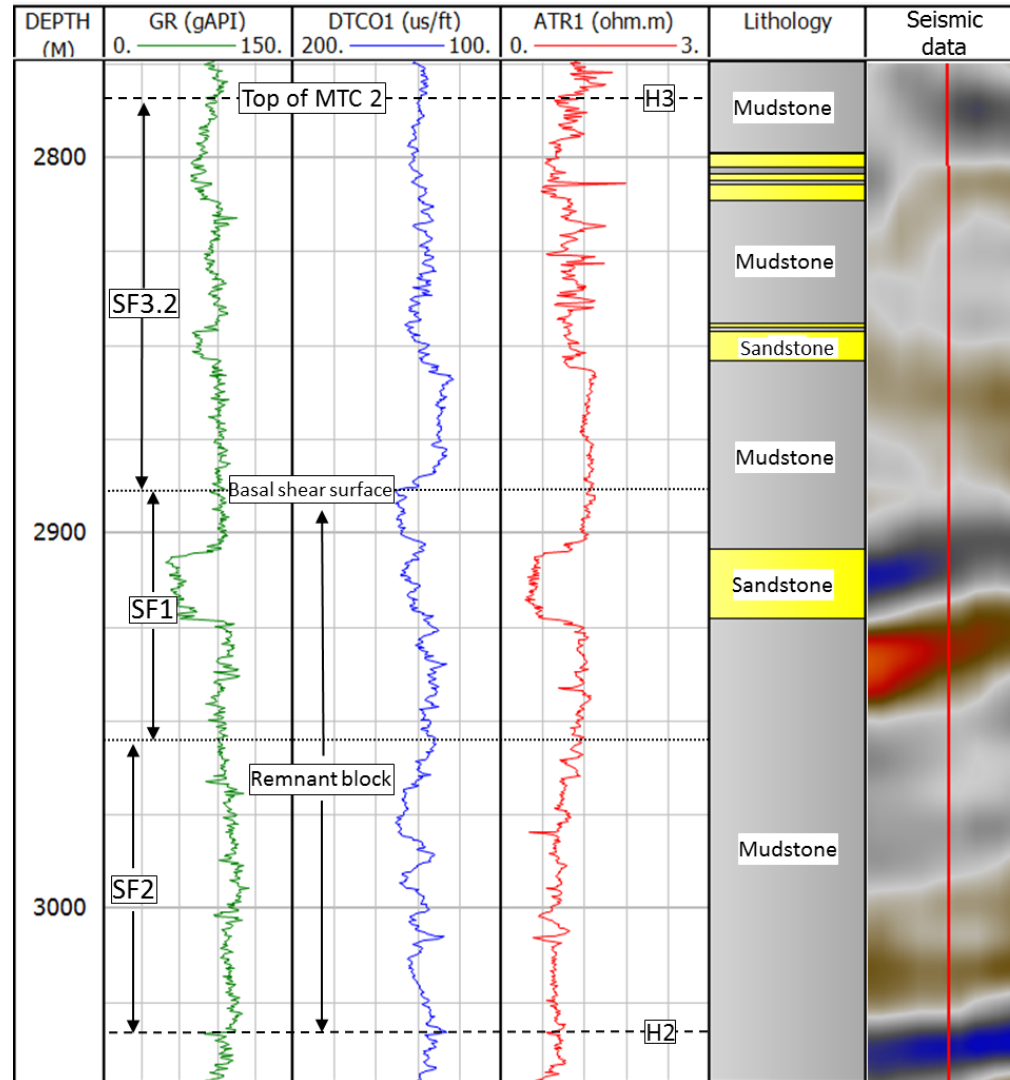


Figure 7B

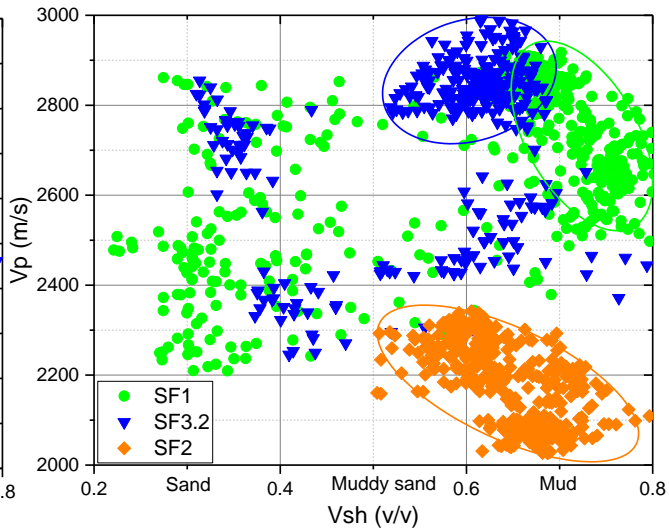
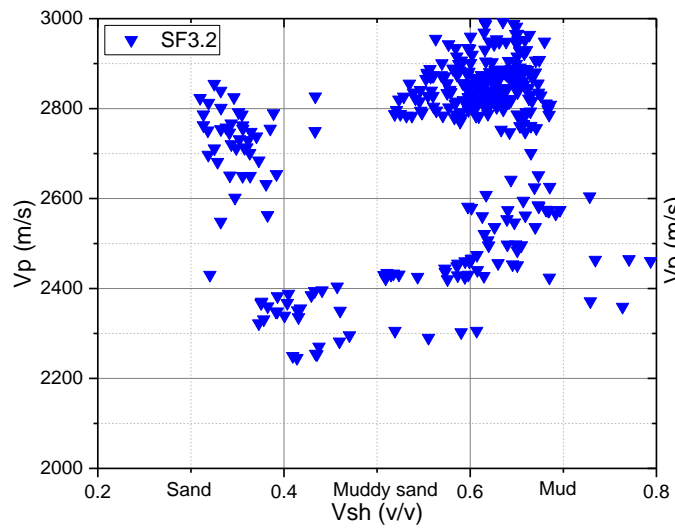
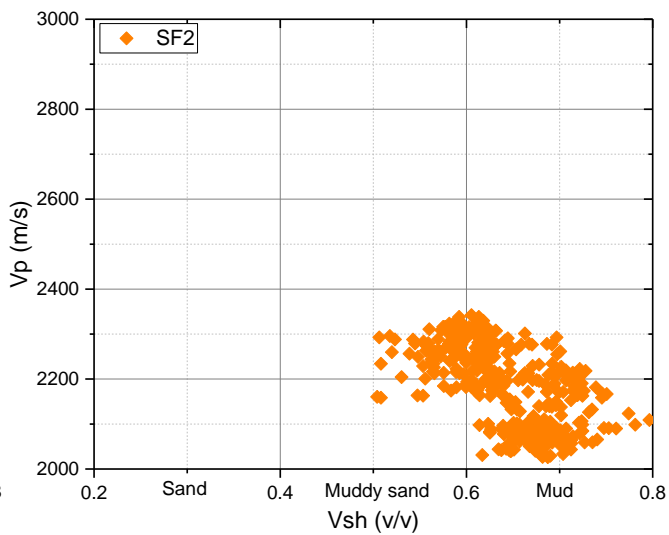
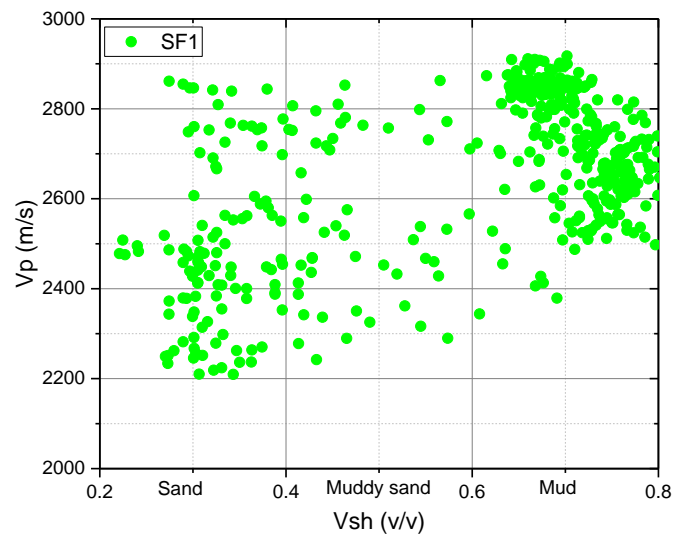


Figure 8A

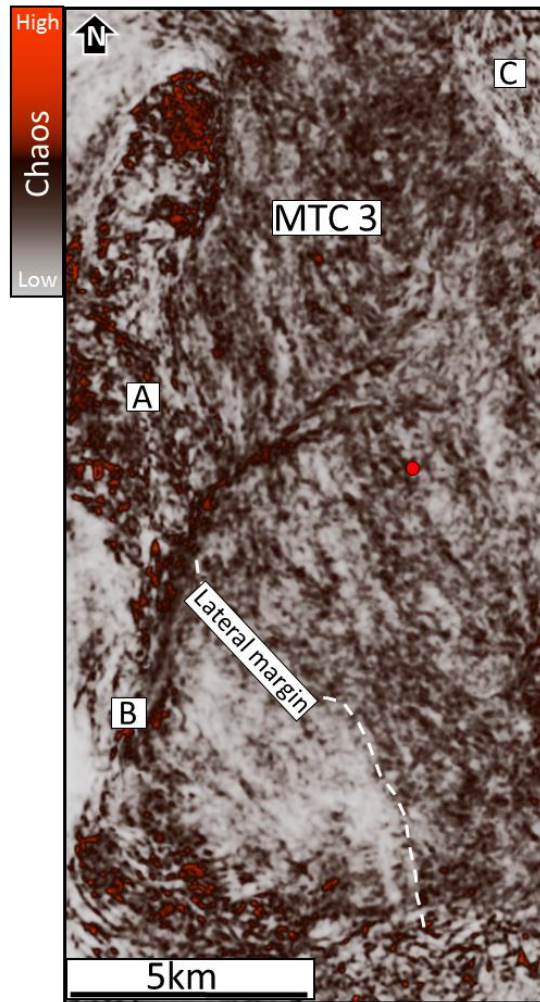


Figure 8B

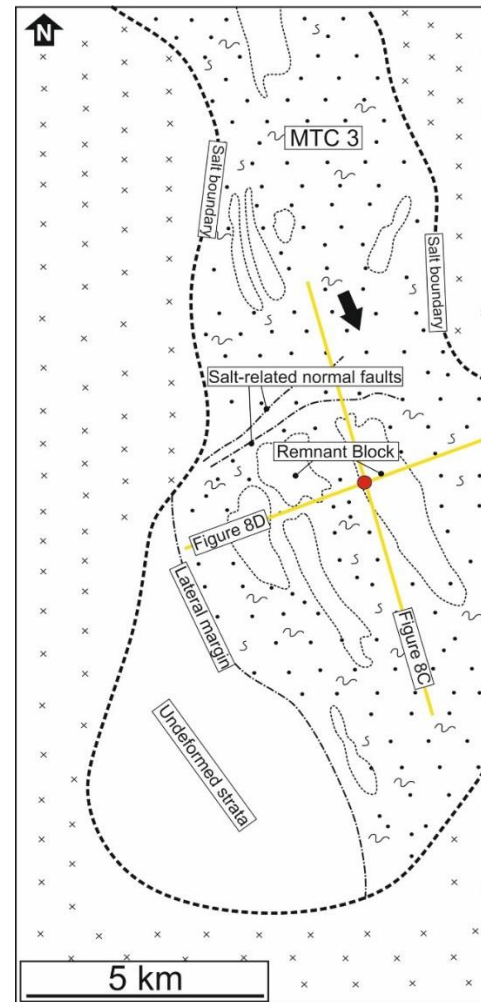


Figure 8C

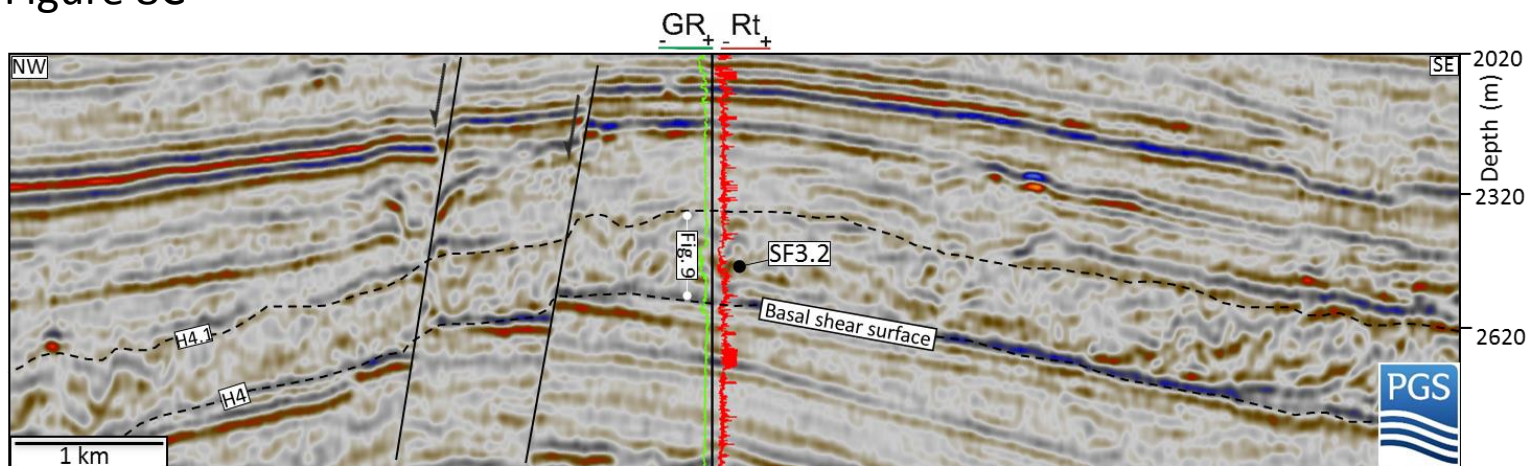


Figure 8D

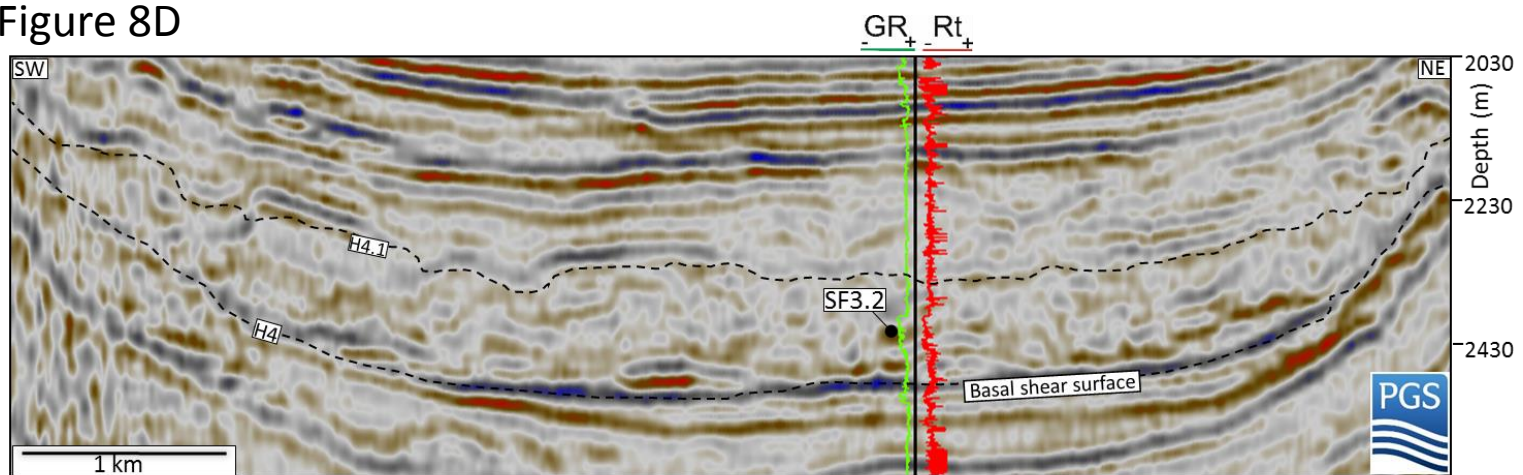


Figure 9A

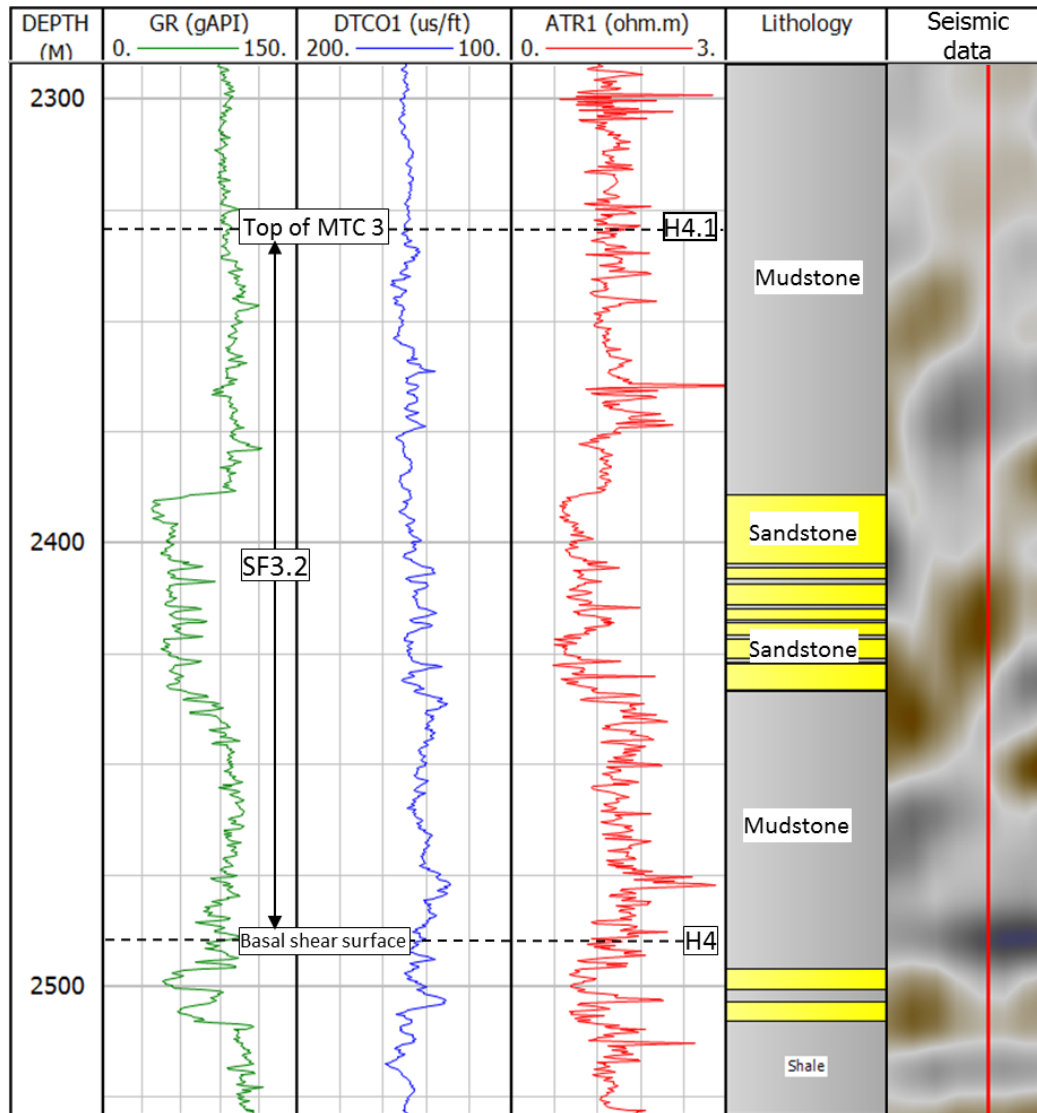


Figure 9B

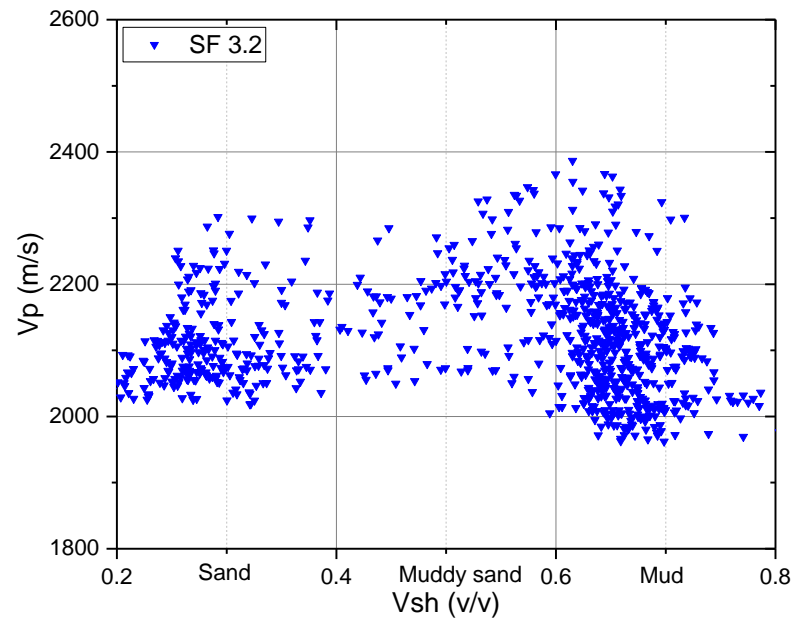


Figure 10A

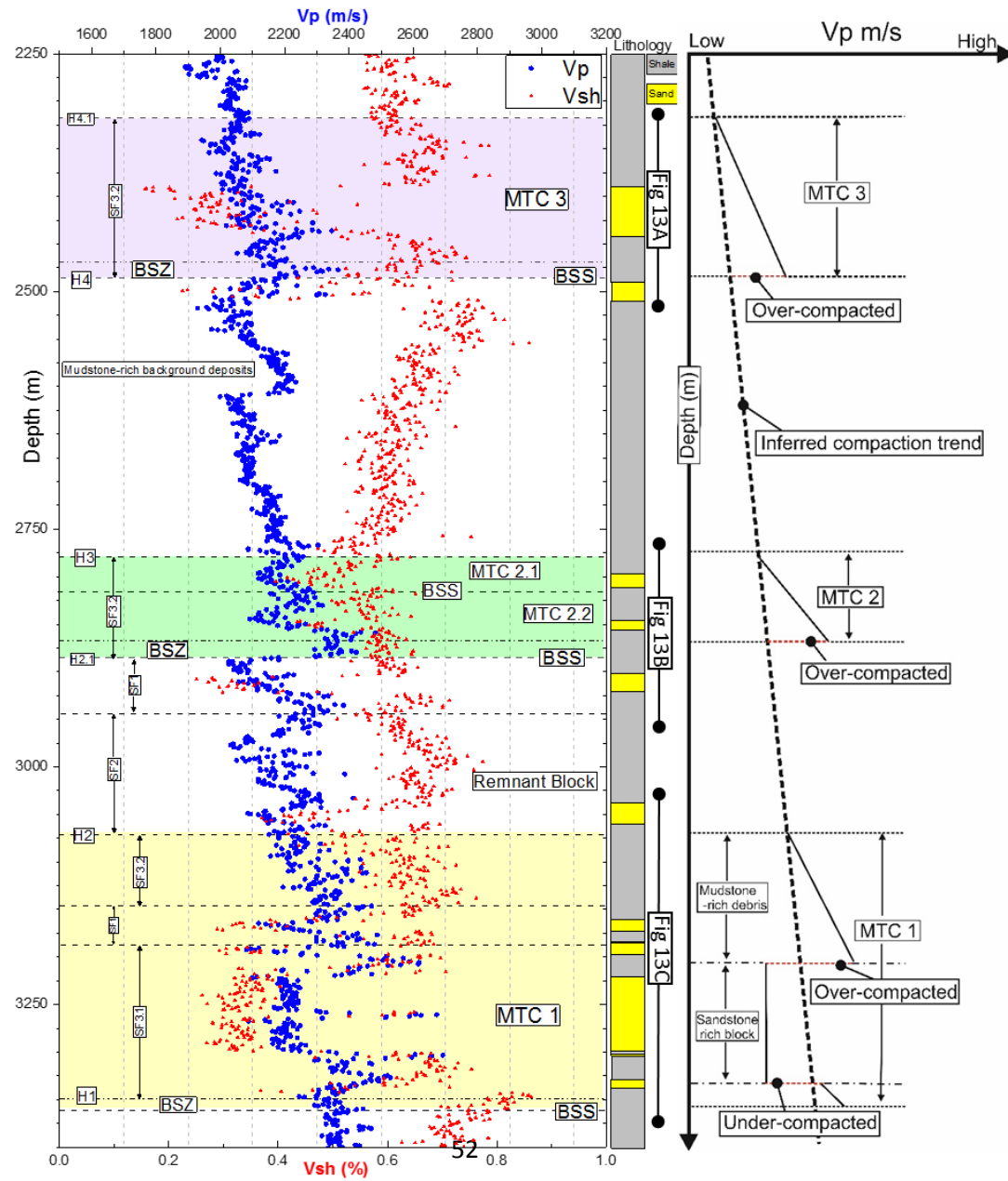


Figure 10B

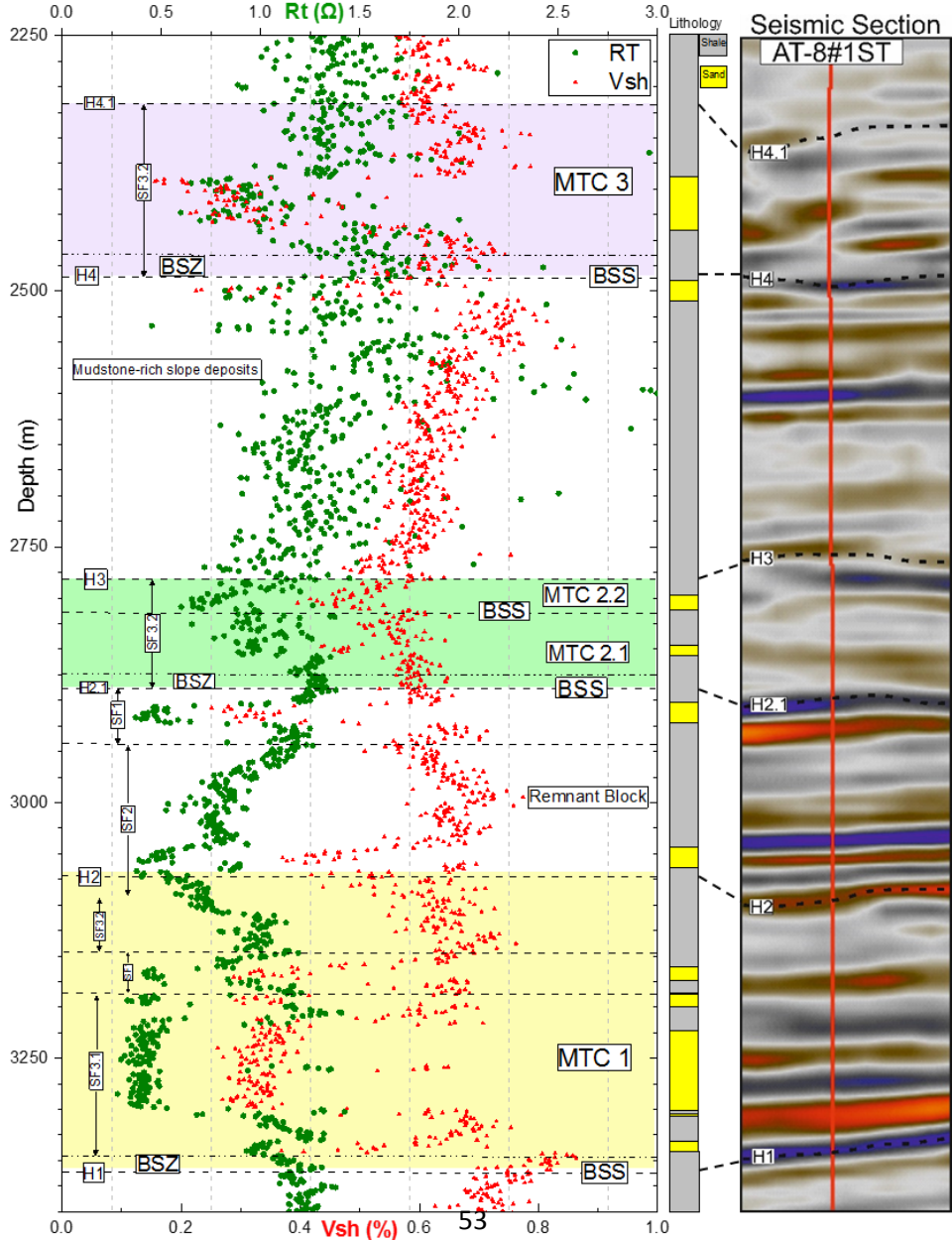


Figure 11A

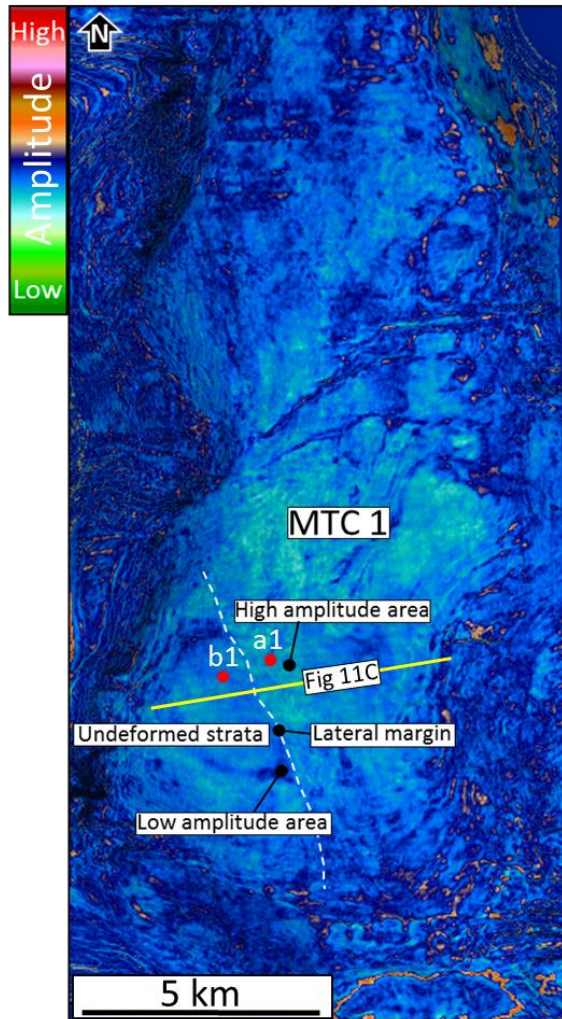


Figure 11B

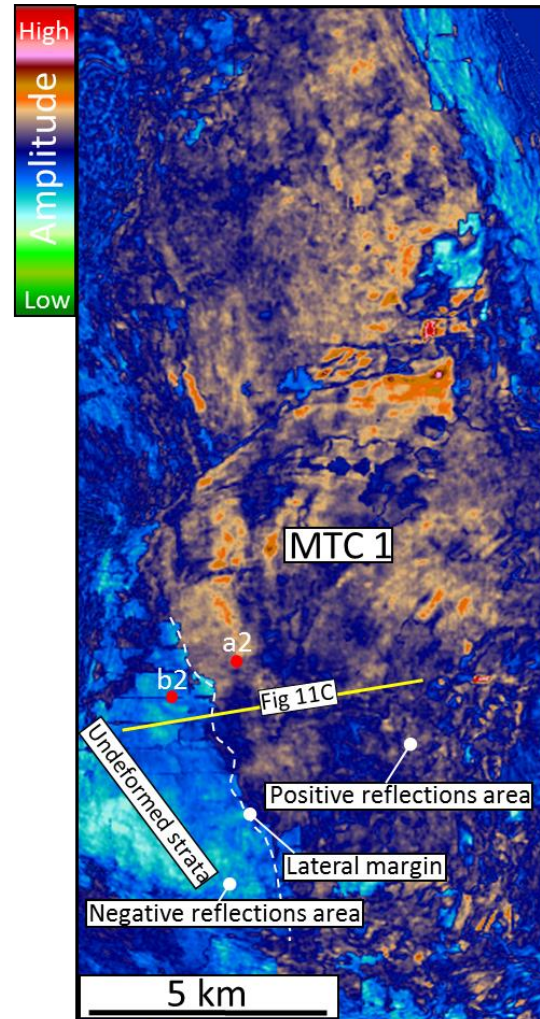


Figure 11C

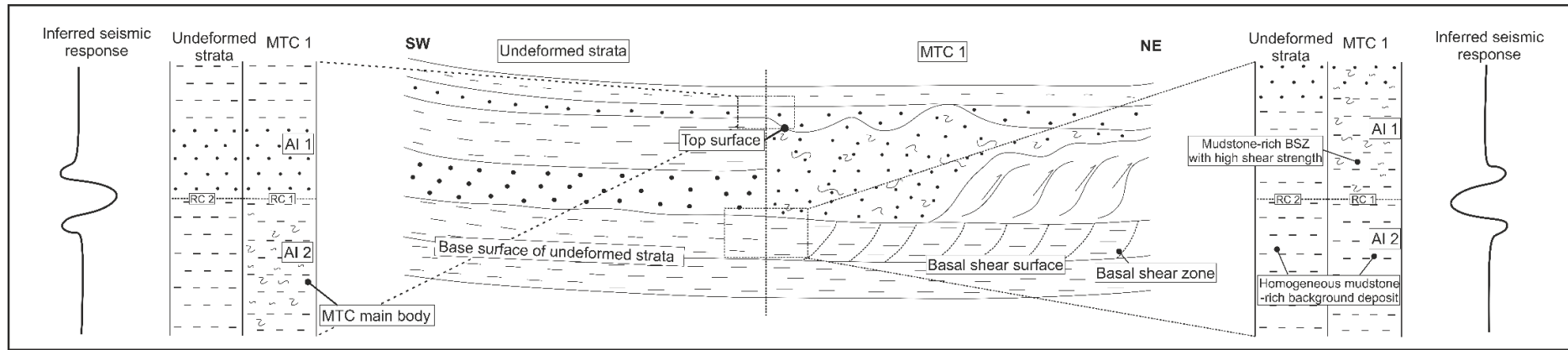


Figure 12A

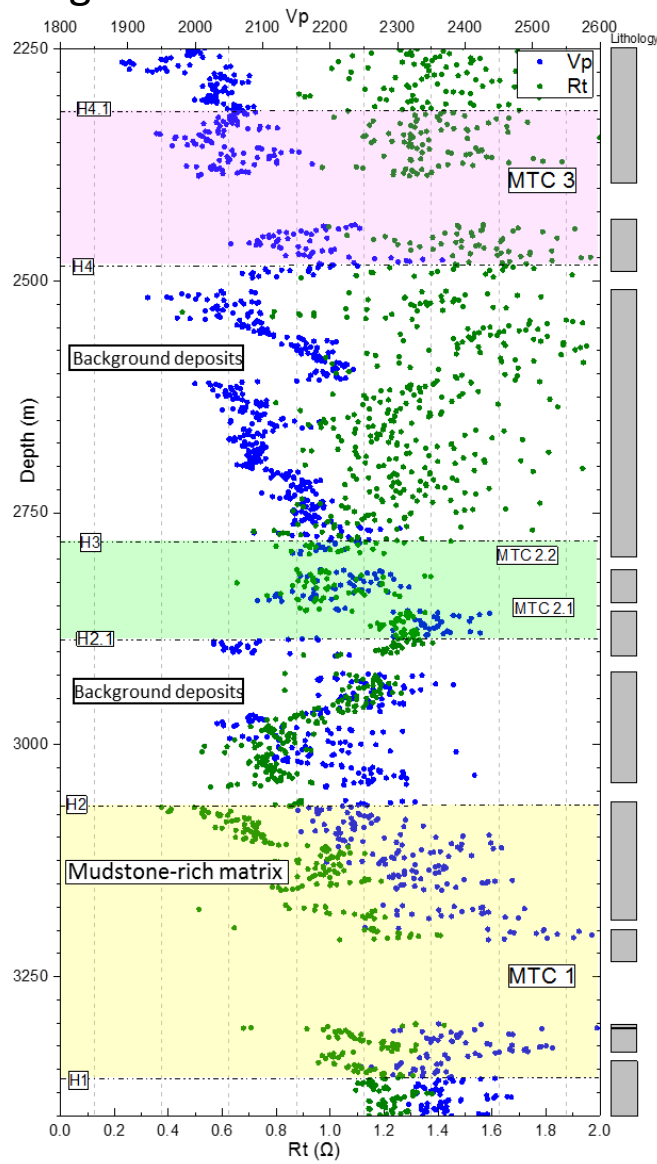


Figure 12B

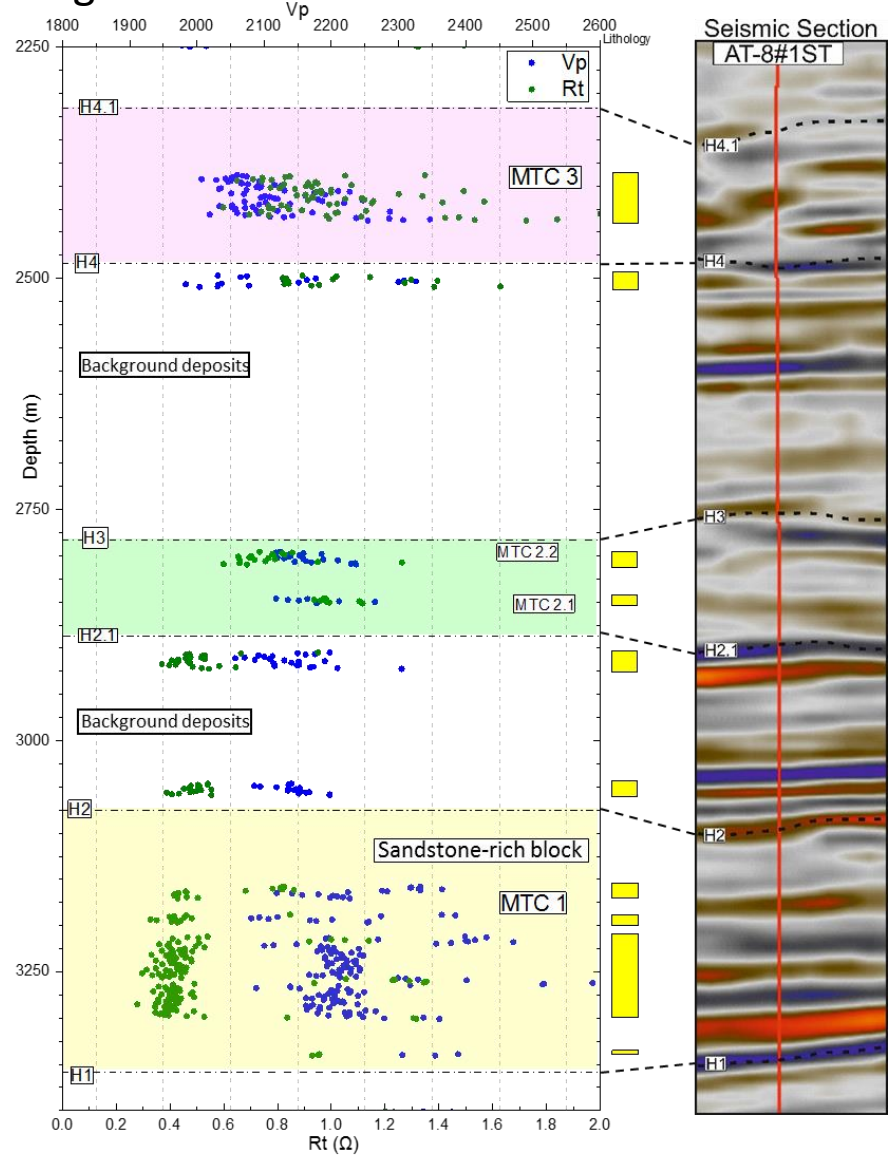


Figure 13A

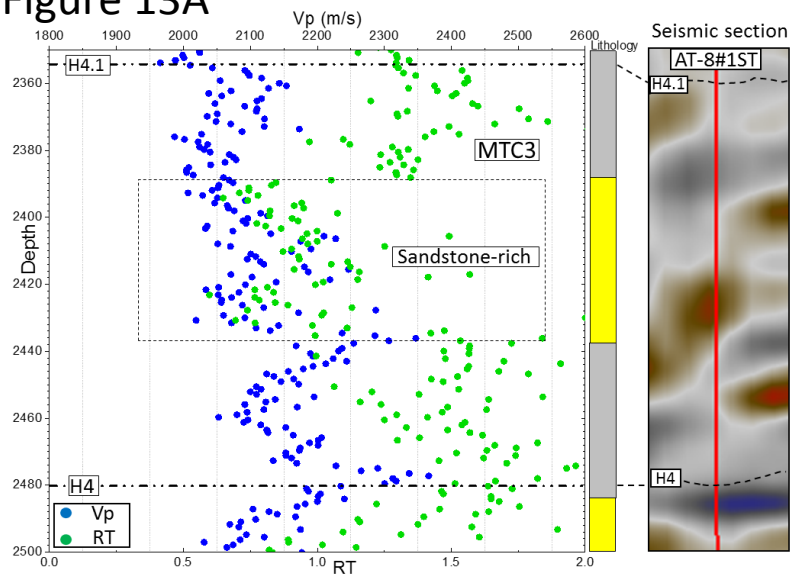


Figure 13B

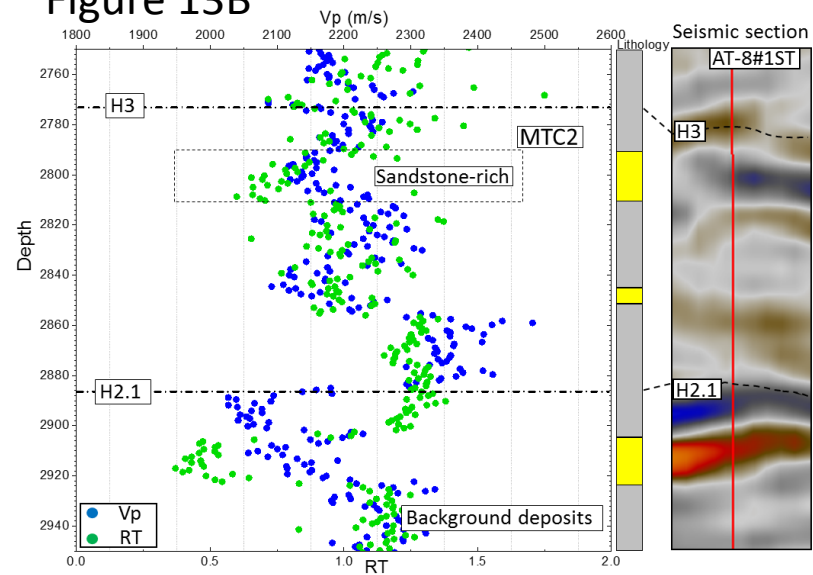


Figure 13C

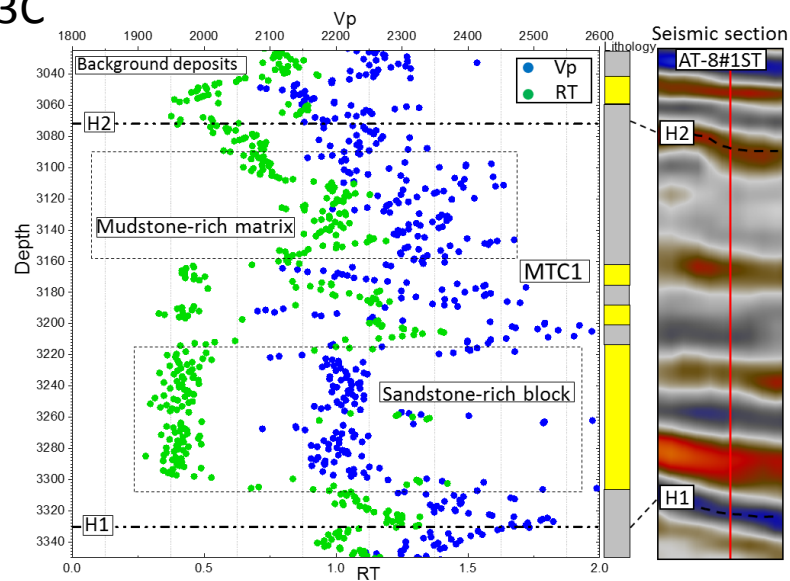


Figure 14

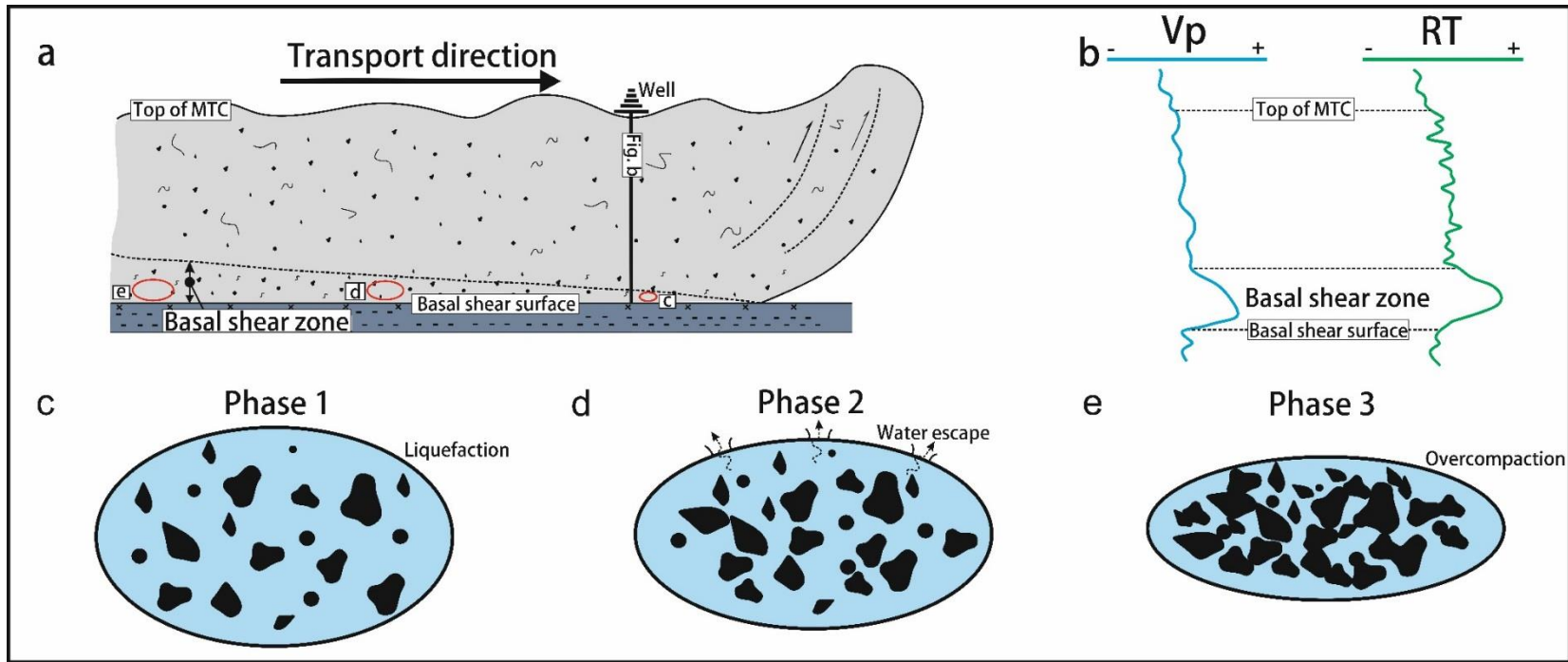


Table 1

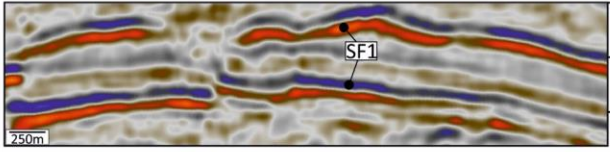

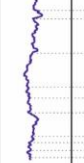
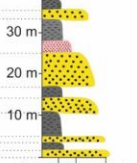
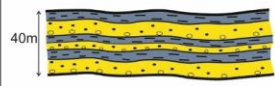
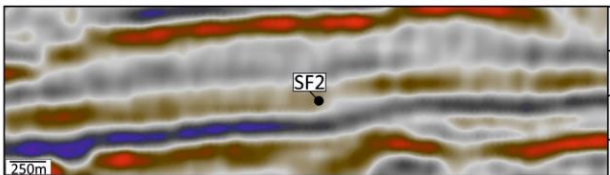


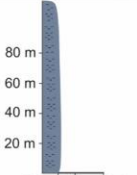
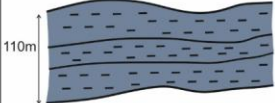
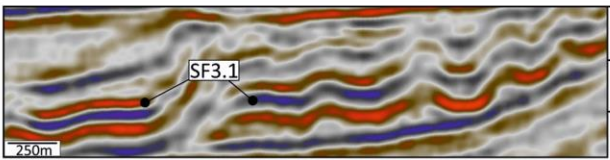

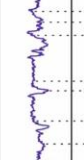
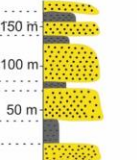
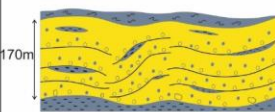
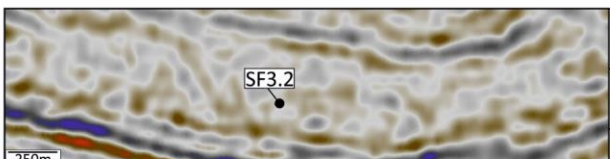

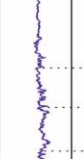
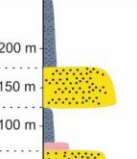
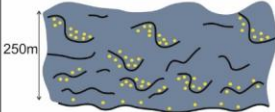
Seismic facies summary							
Types	Seismic sections	GR	Sonic	Lithology	Schematic facies geometries	Facies characteristics	Depositional environment
SF1						Sub-parallel to parallel, fair continuity, high amplitude reflections; seismic reflectors thinning and pitching out to the end. A fining up-ward trend with block low GR response at base and serrated high GR response at top.	Thinly bedded sandstone-rich and mudstone-rich deposits.
SF2						Sub-parallel to parallel reflections, good continuity, with medium to low amplitude reflections; Constantly serrated high GR response.	Background low energy mudstone-rich deposits.
SF3.1						Less deformed, but more continuous, medium to high amplitude reflections; A fining upward trend GR response at base, a set of blocky low GR response at middle, and a fining upward GR response again at top.	Remobilised and transported sandstone-rich blocks
SF3.2						Chaotic reflections, bad continuity with medium to low amplitude reflections; Constantly serrated high GR response or high GR response interbedded with a set of blocky low GR response.	Mixed highly deformed slump deposits with large sandstone-rich blocks.

Table 2

MTC	Thickness (m)	Lithology	Thickness of sandstone rich parts (m)
MTC 1	270 m	Large sandstone-rich blocks with mudstone-rich debris	Approx. 180 m
MTC 2.1	77 m	Mudstone-rich debrite with sandstone-rich blocks	Approx. 30 m
MTC 2.2	43 m	Mudstone-rich debrite	Approx. 10 m
MTC 3	182 m	Mudstone-rich debrite with sandstone-rich blocks	Approx. 70 m